

Summer Internship Report

Design, Simulation, and Experimental Characterization
of a Hydro-Reactive Solid Rocket Motor and Test Bed



भारतीय प्रौद्योगिकी संस्थान हैदराबाद
Indian Institute of Technology Hyderabad

Department of Mechanical and Aerospace Engineering

Energetics and Propulsion Lab

Under the Guidance of

Dr. Gnanaprakash K

Submitted by

Yerra Gowri Shankar Venkata Ashish

2022MEB1367

Department of Mechanical Engineering

Indian Institute of Technology Ropar

Declaration

I declare that this written submission represents my ideas in my own words, and where ideas or words of others have been included, I have adequately cited and referenced the original sources. I also declare that I have adhered to all principles of academic honesty and integrity and have not misrepresented or fabricated or falsified any idea/data/fact/source in my submission. I understand that any violation of the above will be a cause for disciplinary action by the Institute and can also evoke penal action from the sources that have thus not been properly cited, or from whom proper permission has not been taken when needed.

Yerra Gowri Shankar Venkata Ashish

(Name)

2022MEB1367

(Roll No.)

Acknowledgement

I would like to express my heartfelt gratitude to Dr. Gnanaprakash K sir and Indian Institute of Technology Hyderabad for granting me the esteemed opportunity to participate in their Summer Internship program, this internship experience has been profoundly enriching, significantly advancing both my personal and professional development.

I am especially thankful to Dr. Gnanaprakash K for his invaluable guidance and unwavering support throughout the internship. I would also like to convey my sincere gratitude to Deepachanthiran R K (PhD), M. Harshavardhan (M Tech) in IITH for their exceptional mentorship and constructive feedback during my intern period of 8 weeks.

My heartfelt thanks go to my fellow interns for their collaborative ideas, teamwork, and camaraderie, and to my parents for their unwavering encouragement. This work would not have been possible without their collective support.

Contents

Declaration	i
Acknowledgement	ii
1 Introduction	1
1.1 Performance Characteristics	5
2 Propellant Making	6
2.1 Aim	6
2.2 Procedure	6
2.3 Compositions and Measurements	7
2.4 Inferences	7
2.5 Challenges and Solutions	8
2.5.1 Trapped Air, Voids, and Porosity	8
2.5.2 Vacuum Casting	8
2.6 Propellant Cutting	9
2.6.1 Aim	9
2.6.2 Procedure	9
3 Experimental Characterization	11
3.1 Bomb Calorimeter	11
3.1.1 Aim	11
3.1.2 Theory	11
3.1.3 Procedure	12
3.1.4 Observations	13
3.2 Burn Rate Experiment	15
4 Hydrolysis of Aluminum	18
4.1 Introduction	18
4.2 Al-Wire Feeding	18
4.3 Al-Powder Injection	19
4.4 Micronized Powder vs. Wire Feed	20
4.4.1 Challenges	20
4.5 Micronized Aluminum Injection Design	20
4.5.1 Objectives	20
4.6 Proposed Solutions	21
5 Solid Rocket Motor Design Approach	23

5.1	Theory: Chamber Pressure with Propellant Burn and Water Injection	23
5.2	Open Motor Simulation	25
6	Hydro-Reactive Fuel Test Stand	28
6.1	Design of Test Chamber	28
6.1.1	Design Requirements	28
6.1.2	Materials used:	28
6.2	The Mass Ejection Efficiency Test Bed:	29
6.2.1	The Prelimininry design requirements	29
6.2.2	General Stresses in Pressurized Cylinders	29
6.2.3	Maximum Stresses with Internal Pressure Only	29
6.2.4	Longitudinal Stress in Closed-End Cylinders	30
6.3	The Test Bed Design	32
6.3.1	Design Requirements	32
6.3.2	Components and Construction	32
6.3.3	Component Specifications	35
6.4	Design of the Test Chamber	37
6.4.1	Conceptual Design 1: Threaded Joint Assembly	38
6.4.2	Conceptual Design 2: Flange Joint	39
6.5	Madras Test Bed Drawings and Design	40
6.5.1	Design Inspiration and Modifications	40
6.5.2	Water Injection System	42
6.5.3	Performance Analysis from Literature	42
6.6	Modified Drawings and Features	43
6.6.1	Variable Nozzle Mechanism	44
6.6.2	Modified Primary Chamber Nozzle	45
7	Design Calculations	46
7.1	Stress Concentration Factor Calculations	47
7.1.1	Stress Concentration near Injection Holes	47
7.1.2	Stress Concentration near Fillet to Flange	49
7.2	Failure Theory Analysis	49
7.2.1	Von Mises Stress Theory	49
7.2.2	Maximum Shear Stress (MSS) Theory	49
7.2.3	Failure Analysis Results Table	50
7.3	Fatigue Analysis	50
7.3.1	Theory and Formulas	50
7.3.2	Analysis Results	51
7.4	Transient Heat Conduction: Lumped Analysis	52
7.4.1	Theory and Formulas	52
7.4.2	Lumped Analysis Calculations	53
7.5	Thermal Stress Analysis	54
7.5.1	Theory and Material Properties	54
7.5.2	Thermal Stress Calculation Results	54
8	Simulation	56
8.1	Simulation	56
8.1.1	Analysis simulation Procedure	56
8.1.2	Simulation Results	56

9 Views of the Test Bed	58
References	62

List of Figures

1.1	Classification of Propulsive Devices	1
1.2	Characteristics of Some Operational Solid propellants	2
1.3	Bimodal packing of Ammonium Perchlorate (AP) particles.	2
1.4	Curing reaction mechanism for HTPB + TDI.	4
1.5	Typical thrust vs. time curve for a solid rocket motor.	5
2.1	Compositions prepared	7
2.2	Metal Hydride propellant prepared	7
2.3	Weight of Sample After Curing	8
2.4	Industrial vacuum casting setups	9
2.5	Cutting the propellant grain into uniform samples.	10
3.1	Bomb Calorimeter Setup	11
3.2	The key components: differential thermometer, electrical connections, Nichrome wire, cotton thread, calorimeter, and crucible.	13
3.3	Calorific Values for different compositions	13
3.4	A schematic of the granular diffusion flame model for solid propellant combustion. It illustrates how heat is conducted from the flame back to the surface, sustaining the reaction.	15
3.5	A graph showing the relationship between burn rate and pressure for various pressure exponents (n), as described by the burn rate law, $r = aP^n$. .	15
3.6	Strand burner setup with camera and chamber	17
3.7	Sequential video frames showing flame front during strand burn	17
4.1	(a) Schematic of the hydrogen generation setup using Ni-Al alloy in NaOH solution. (b) Graph showing hydrogen evolution rate at different temperatures ,Peak occurs at 60 °C	19
4.2	Hydrogen flow rate vs. time for H-2 aluminum powder at 90 °C, 115 °C, and 150 °C, showing increased production with temperature.	19
4.3	Graphs illustrating hydrogen yield from aluminum powder hydrolysis.	20
4.4	Exploded CAD view showing internal components of the pneumatic injection setup.	21
4.5	CAD model of a pneumatic injector assembly with syringe fully inserted into the reactor chamber.	22
5.2	OpenMotor GUI for rocket motor simulation.	25
5.3	Defining propellant properties and grain geometry in OpenMotor.	26
5.4	Nozzle properties inside OpenMotor.	26
5.1	Solid Rocket Motor Design Approach	27

6.1	Stresses in a pressurized cylinder.	29
6.2	Tangential and radial stress distribution for internal pressure only.	30
6.3	A typical setup for a Solid Rocket Motor (SRM) firing test.	31
6.4	A detailed CAD model of the SRM assembly, showing internal components and support structures.	31
6.5	An alternative CAD view, highlighting the nozzle section and external connections.	32
6.6	CAD views illustrating the 3-DOF adjustment capabilities of the test bed, including height (y-axis) [1], lateral position (z-axis)[3], and miniature linear guides[2] for smooth and precise movement	33
6.7	4	33
6.8	DOF along y (5), DOF along z (6), and a slot to adjust and hold position along y direction (7).	34
6.9	Slot to adjust the displacement along z (8)	34
6.10	The complete test bed assembly, highlighting the linear guide rail (9) which allows for longitudinal adjustment along the x-axis.	35
6.11	Product overview for the ARC series profile rail linear guides, showing key features such as a load capacity of 9.7 to 112.8 kN and construction from alloy steel.	35
6.12	A 30-30 series aluminum T-slot extrusion is used for the base support frame.	36
6.13	CAD model of a support leg, designed to be machined from AISI 1080 steel.	36
6.14	CAD model and specifications for the selected NTS series T-slot nuts. . .	37
6.15	Cross-section of the conceptual threaded design. As the main nut is tightened, the chambers are pulled together, compressing the O-rings to create a seal.	38
6.16	An isometric view of the thread joint test chamber assembly.	39
6.17	CAD model of the test chamber assembly using bolted flange joints between the primary chamber, secondary chamber, and nozzle section. . . .	39
6.18	Isometric view of the Madras Test Bed CAD assembly.	40
6.19	Technical drawings of the thrust chamber and intermediate plate that was referenced.	41
6.20	Water injection system schematic and CAD implementation.	42
6.21	Performance graphs from literature illustrating the effect of injection angles.	43
6.22	Cross sectional view of modified test bed.	44
6.23	A detailed cross-sectional view of the variable nozzle, showing the threaded adjustment mechanism and sealing O-rings.	45
6.24	Front view dimensions for the modified primary chamber nozzle insert. .	45
7.1	Identification of critical stress areas.	47
7.2	Stress-concentration factor (K_t) for a bar in tension with a transverse hole (Figure A-15-1).	48
7.3	Stress-concentration factor (K_t) for a round shaft with a shoulder fillet in tension (Figure A-15-7).	49
7.4	Material properties and the resulting S-N fatigue curve.	52
7.5	Temperature-time response for the primary and secondary chambers, plotted using lumped-analysis. Time constants of $\tau_1 \approx 555\text{ s}$ (primary) and $\tau_2 \approx 350\text{ s}$ (secondary).	53

8.1	Preliminary FEA results for the primary chamber flange, showing temperature and stress distributions.	57
9.1	Isometric view of the full test bed assembly, the pressure chamber mounted on the adjustable supports and linear guide rail.	58
9.2	A partially sectioned isometric view, highlighting the pressure chamber, intermediate plate and nozzle assembly	59
9.3	Orthographic side and top views of the test bed assembly.	60
9.4	Orthographic front and rear views of the assembly.	61

List of Tables

1.1	Example Propellant Compositions	3
2.1	Volume and Density Measurements for Selected Compositions	7
3.1	Calorific Value Measurements of Bimodal Compositions	13
6.1	Calculation of Hoop, Radial, and Longitudinal Stresses (σ_y (AISI 1080) = 400MPa)	30
7.1	Calculation of Hoop, Radial, and Longitudinal Stresses (σ_y (AISI 1080) = 400MPa)	46
7.2	Calculation of Stress Concentration Factors at Injection Holes.	48
7.3	Calculation of Stress Concentration Factor at the Flange Fillet.	49
7.4	Comparison of Design Factors from Von Mises and MSS Theories.	50
7.5	Fatigue Analysis Calculations and Results.	51
7.6	Calculation of Biot Number and Time Constant.	53
7.7	Thermal Stress Analysis Results for Key Components.	55

Chapter 1

Introduction

Newton's third law of motion, 'For every action, there is an equal and opposite reaction,' is the only way humans have ever figured out of getting somewhere in space is by pushing something away. The action of pushing against something, or ejecting away something gives us the ability to propel forward, there are several ways of harnessing energy to eject the matter at high velocities and produce thrust, and solid rocket propulsion is one of kinds, where chemical energy of the solid propellant is harnessed to eject mass and produce thrust.

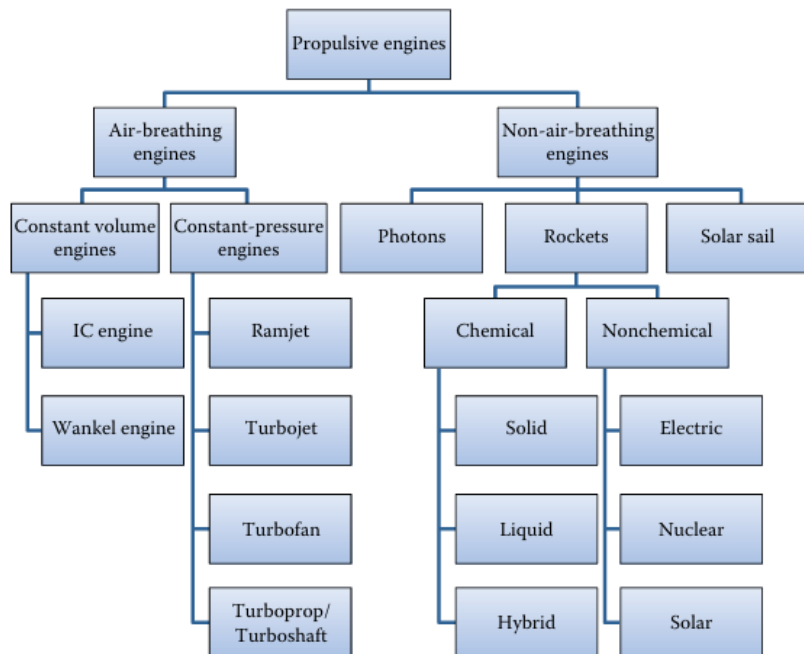


Figure 1.1: Classification of Propulsive Devices

In solid rocket propulsion chemical energy released as reactants reach a more stable state through a redox reaction, is harnessed to generate thrust. A typical solid rocket propellant consists of fuel and oxidizer held together in a solid matrix by a binder, with a curing agent added to shape and harden the grain.

Propellant Type ^a	I_s Range (sec) ^b	Flame Temperature ^c		Density or Spec. Gravity ^c (lbm/in ³) (SG)	Metal Content (mass %)	Burning Rate ^{c,e} (in./sec)	Pressure Exponent ^e n	Hazard Classification ^d	Stress (psi)/Strain (%)		Typical Processing Method	
		(°F)	(K)						-60°F	+150°F		
DB	220–230	4100	2550	0.058	1.61	0	0.05–1.2	0.30	1.1	4600/2	490/60	Extruded
DB/AP/AI	260–265	6500	3880	0.065	1.80	20–21	0.2–1.0	0.40	1.3	2750/5	120/50	Extruded
DB/AP-HMX/AI	265–270	6700	4000	0.065	1.80	20	0.2–1.2	0.49	1.1	2375/3	50/33	Solvent cast
PVC/AP/AI	260–265	5600	3380	0.064	1.78	21	0.3–0.9	0.35	1.3	369/150	38/220	Cast or extruded
PU/AP/AI	260–265	5700	3440	0.064	1.78	16–20	0.2–0.9	0.15	1.3	1170/6	75/33	Cast
PBAN/AP/AI	260–263	5800	3500	0.064	1.78	16	0.25–1.0	0.33	1.3	520/16 (at -10°F)	71/28	Cast
CTPB/AP/AI	260–265	5700	3440	0.064	1.78	15–17	0.25–2.0	0.40	1.3	325/26	88/75	Cast
HTPB/AP/AI	260–265	5700	3440	0.067	1.86	4–17	0.25–3.0	0.40	1.3	910/50	90/33	Cast
HTPE/AP/AI	248–269	5909	3538	0.07	1.70		0.4–0.7	0.50	1.3	174/44 (77°F)		Cast
PBAA/AP/AI	260–265	5700	3440	0.064	1.78	14	0.25–1.3	0.35	1.3	500/13	41/31	Cast
AN/Polymer	180–190	2300	1550	0.053	1.47	0	0.06–0.5	0.60	1.3	200/5	NA	Cast

Figure 1.2: Characteristics of Some Operational Solid propellants

APCP(Ammonium Perchlorate Composite Propellant) is a composite propellant with high ISP(Specific Impulse) values and proven reliability and ease of fabrication it is widely used in SRBs. APCP is heterogeneous solid formulation in which finely powdered solid ingredients are bound together in a polymer matrix. Fundamentally, it consists of three principal components:

1. **Oxidizer (60–70 wt %):** Typically, ammonium perchlorate (AP), Upon heating, AP decomposes to release oxygen, which then reacts with the fuel phase to sustain combustion.

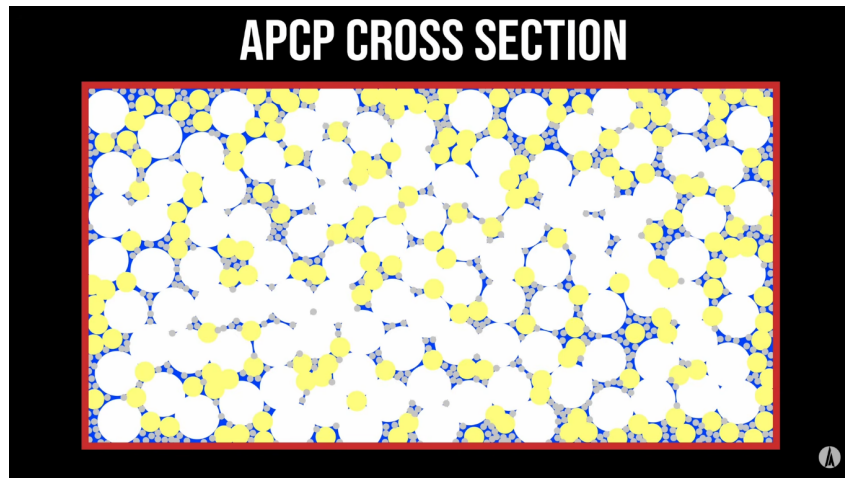


Figure 1.3: Bimodal packing of Ammonium Perchlorate (AP) particles.

A bimodal AP distribution uses coarse (400 µm) grains for the primary load-bearing structure and fine (40 µm) grains to occupy the voids between them.

- i. Filling interstitial spaces maximizes propellant density and minimizes porosity, boosting overall energy per unit volume.
- ii. Tighter packing improves mechanical integrity, reducing crack initiation and propagation under thermal or mechanical stress.
- iii. Uniform packing also promotes more consistent regression rates and flame propagation, enhancing thrust stability.

2. **Fuel (15–20 wt %)**: Most often aluminum powder. Aluminum's high enthalpy of oxidation raises flame temperature and increases exhaust velocity, thereby boosting specific impulse. The energy content of the propellant is proportional to the composition of the metal.
- i. Aluminum is favored in composite propellants for its exceptional gravimetric (31 MJ/kg) and volumetric energy density (2.7 g/cm³).
 - ii. Its combustion produces flame temperatures above 3000 K, boosting exhaust velocity and specific impulse.
 - iii. Fine Al powders (1–100 µm) disperse uniformly in binders like HTPB, enabling rapid, efficient burn and robust grain mechanics.
 - iv. Aluminum is non-hygroscopic, non-toxic, and benefits from well-established handling, processing, and safety protocols.
 - v. Magnesium is added to lower ignition temperature and elevate initial flame temperatures (3500 K), improving Al vaporization and flame spread.
 - vi. Mg also enhances burn-rate sensitivity, reduces Activation energy and molten slag, nozzle erosion, and synergistically increases overall combustion completeness.

Metal-rich propellants demand very high ignition temperatures and co-additives (e.g., Mg) to reliably initiate combustion, while two-stage aluminum oxidation promotes agglomeration and slag that fouls the nozzle. High metal loadings (>50 wt %) create local fuel-rich pockets and condensed-phase heat sinks, lowering flame temperatures and combustion completeness. Their steep pressure sensitivity ($r = a P^n$) also makes burn rates prone to instabilities like chuffing or high-frequency oscillations.

Table 1.1: Example Propellant Compositions.

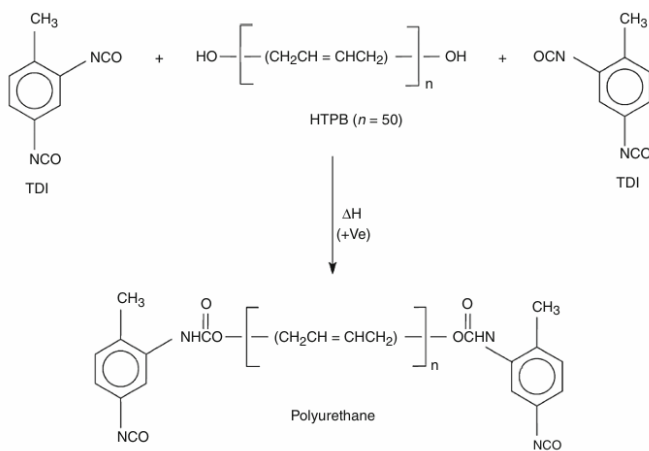
25gms	Component	10Al-40Mg (%)	25Al-25Mg (%)
Metal(fuel)	Metal(fuel)	50	25 25
Oxidiser	AP	36	28.8 7.2
Fuel and Binder	HTPB	11.2	11.2
Plasticiser	DOA	2.1	2.1
Curing Agent	TDI	0.7	0.7
	Total	100	100

3. **Binder/Fuel (10–20 wt %)**: A polymer such as hydroxyl-terminated polybutadiene (HTPB) that both holds the solid ingredients in a mechanically robust grain and participates as a secondary fuel. The binder is mixed with a curing agent to form a cross-linked, elastomeric network.

Function of Components in Binder

- i. Loose metal (Al and Mg) and oxidizer (APCP) particles are mechanically encapsulated and bound by van der Waals forces within the cured HTPB polymer matrix.
- ii. TDI isocyanate groups ($-\text{N}=\text{C}=\text{O}$) react with HTPB terminal hydroxyl groups ($-\text{OH}$), forming urethane linkages ($-\text{NH}-\text{C}(=\text{O})-\text{O}-$) in a cross-linking reaction.
- iii. Each TDI molecule, bearing *two* isocyanate groups, bridges multiple HTPB chains, creating a 3D polymer network that encapsulates oxidizer (e.g., ammonium perchlorate) and fuel (e.g., aluminum powder).

Fig. 4 Curing reaction mechanism for HTPB + TDI



Springer

Figure 1.4: Curing reaction mechanism for HTPB + TDI.

- iv. Because aluminum particles have smooth surfaces, surfactants or coupling agents (e.g., MAPO) may be required to improve HTPB wetting and adhesion.
- v. The cured matrix becomes a *flexible, rubbery solid* that binds all components, providing mechanical integrity and controlled-burn characteristics.
 - a) HTPB provides structural support, toughness, and shock resistance to the propellant grain.
 - b) Dioctyl adipate (DOA) acts as a plasticizer, increasing flexibility and reducing the risk of thermal cracking.
 - c) Toluene diisocyanate (TDI) acts as a curing agent, cross-linking HTPB chains through urethane bonds to form a resilient three-dimensional polymer network.

1.1 Performance Characteristics

Total Impulse

Although *thrust* is an important parameter for characterizing the *lift capability* of a rocket motor, it provides no indication of the how high the rocket will be propelled. For this, one needs a measure of the *total output* in terms of propulsion capability. The essential parameter for this is the **Total Impulse** of the rocket motor, which incorporates the essential element of time, or thrust duration. Total Impulse is defined as the time integral of the thrust over the operating duration of the motor:

$$I_t = \int F(t)dt$$

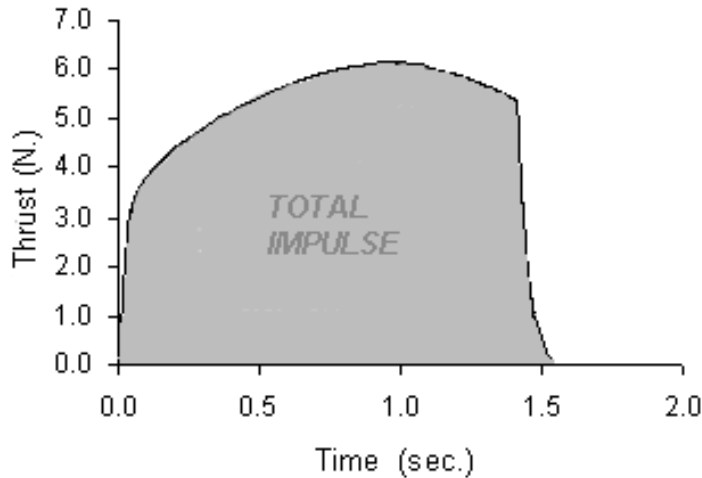


Figure 1.5: Typical thrust vs. time curve for a solid rocket motor.

Specific Impulse ($I_{sp} = V_e/g_0$)

Specific Impulse can be considered to relate the *thrust produced by a unit mass* (e.g. 1 lb or kg) of propellant over a *burning time of one second*. The units in seconds(s) , can also be interpreted as the thrust generated by propellant of 0.1kg mass in one second .

$$I_{sp} = \frac{I_t}{w_p}$$

Delivered specific impulse has a dependency upon:

- (a) Mass flowrate, and thus on motor size
- (b) Available combustion energy of the propellant
- (c) Nozzle efficiency
- (d) Ambient pressure conditions
- (e) Heat loss to the motor hardware
- (f) Two-phase flow losses
- (g) Combustion efficiency

Chapter 2

Propellant Making

2.1 Aim

To precisely fabricate propellants with specified compositions in order to investigate their properties and performance parameters.

2.2 Procedure

- i. Precisely measure the required amount of hydroxyl-terminated polybutadiene (HTPB) into a beaker cleaned with acetone.
- ii. Add the calculated amount of dioctyl adipate (DOA) to the HTPB to reduce viscosity and aid in uniform mixing.
- iii. Add components in ascending order of their size, starting with precisely adding micronized Al, Mg to the mixture while stirring. After all metal powders are added, continue mixing for 20 minutes.
- iv. Add fAP and then add cAP mix thoroughly for 15-20mins, to ensure homogeneity.
- v. Place the mixture in a desiccator to remove air bubbles, and then add TDI and mix thoroughly for 30-40mins.
- vi. Coat the inner walls of the casting chamber with castor oil, pour in the mixed slurry, level the surface, place a weight on top, and keep the assembly under vacuum in the desiccator to eliminate any remaining air.
- vii. Place the filled casting chamber in an oven maintained at 55°C and allow it to cure.
- viii. After a week of curing, carefully extract the propellant grain from the mold without damaging the surface and measure the dimensions of the grain with a vernier caliper and calculate the volume.
- ix. Measure the mass of the propellant grain, and calculate the density.
- x. Make inferences about the readings, and examine the grain for defects such as porosity or incomplete curing. Record all measurements and observations, assign a tag, and prepare it for the next stage of testing.

2.3 Compositions and Measurements

	Component	10Al-40Mg (%)	25Al-25Mg (%)	20Al-20Mg (%)	30Al-30Mg (%)	50Mg (%)	50Al(%)
Metal(fuel)	Metal(fuel)	50	25	20	30	0	50
			25	20	30	50	0
Oxidiser	AP	36	28.8	36.8	20.8	0	0
			7.2	9.2	5.2	36	36
Fuel and Binder	HTPB	11.2	11.2	11.2	11.2	11.2	11.2
Plasticiser	DOA	2.1	2.1	2.1	2.1	2.1	2.1
Curing Agent	TDI	0.7	0.7	0.7	0.7	0.7	0.7
	Total	100	100	100	100	100	100

Figure 2.1: Compositions prepared

10gms	Component		Weight(gms)
Metal(fuel)	Al	10	1
	LiAlH4	5	0.5
Oxidiser	Fine AP	30	3
		35	3.5
Fuel and Binder	HTPB	16	1.6
Plasticiser	DOA	3	0.3
Curing Agent	TDI	1	0.1
	Total	100	10

Figure 2.2: Metal Hydride propellant prepared

Table 2.1: Volume and Density Measurements for Selected Compositions

Composition	Mass (g)	Length (mm)	Diameter (mm)	Volume (mm ³)	Density (kg/m ³)
20Al–20Mg	25.0763	31.03	24.96	15189.22	1650.93
25Al–25Mg	18.2631	24.15	25.04	11897.36	1535.06
30Al–30Mg	17.3129	21.94	25.08	10843.17	1596.66

2.4 Inferences

- (a) As the metal fraction rises from 40 wt % (20Al–20Mg) to 60 wt % (30Al–30Mg), the grain length decreases from 31.0 mm to 21.9 mm and volume shrinks from 15.2 cm³ to 10.8 cm³, indicating the higher average density of metal-rich mixtures.
- (b) The apparent density peaks at 1651 kg/m³ for the 40 % metal blend, drops to 1535 kg/m³ at 50 % metal, then partially recovers to 1597 kg/m³ at 60 % metal, showing a nonlinear relation between dense AP, lighter binder, and metal load.

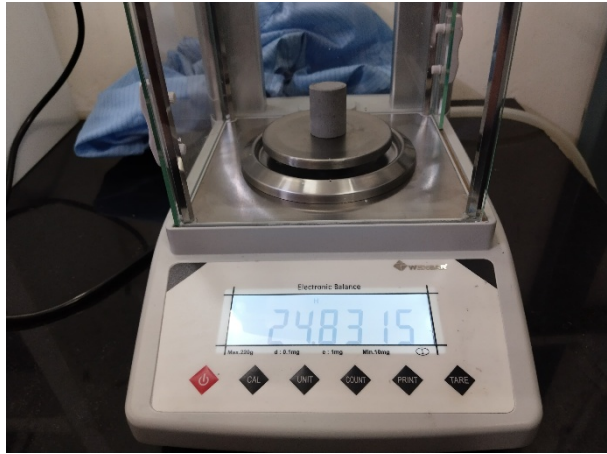


Figure 2.3: Weight of Sample After Curing

(c) Mass measurement stays closest to the 25g target in the lowest metal sample (error 0.3 while higher metal loadings introduce larger weighing and packing variations.

2.5 Challenges and Solutions

2.5.1 Trapped Air, Voids, and Porosity

During the mixing and casting of solid propellants, the viscous binder system traps air bubbles within the slurry. These trapped air pockets/layers lead to internal porosity in the cured grain, which leads to weak mechanical strength and uneven combustion rates.

2.5.2 Vacuum Casting

Vacuum casting is the process where the propellant mixture is placed in a vacuum chamber, where pressure is reduced to encourage the expansion and escape of entrained air. Once air bubbles are removed, the degassed slurry is poured into a mold under vacuum to ensure consistent grain geometry and curing.

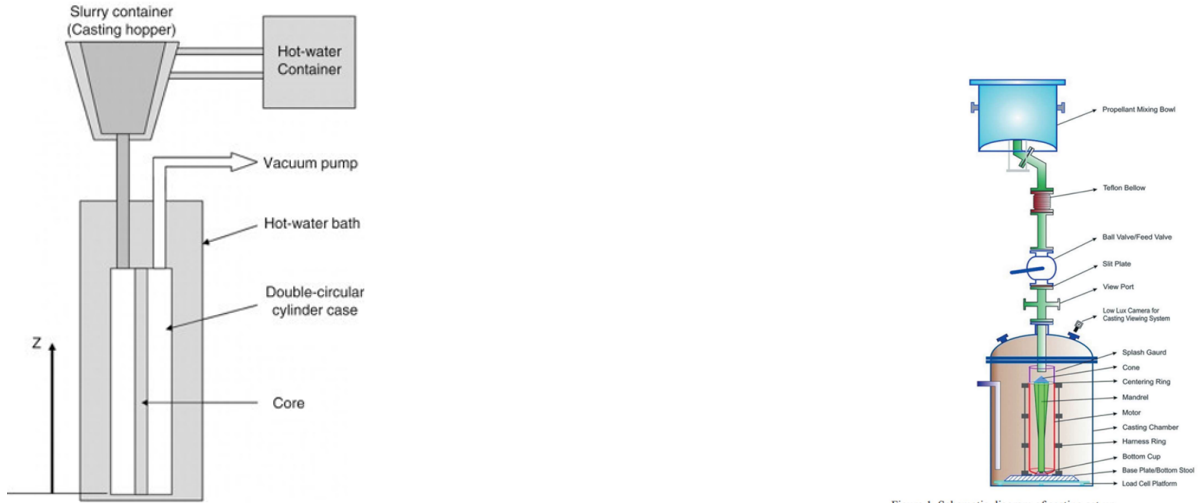


Figure 1. Schematic diagram of casting set-up.

(a) Industrial vacuum casting setup.

(b) Vacuum casting schematic

Figure 2.4: Industrial vacuum casting setups

2.6 Propellant Cutting

2.6.1 Aim

Cutting propellant samples precisely into desired dimensions for experimental studies. Standardizing sample geometry and size maximizes repeatability and statistical confidence in burn-rate experiments.

2.6.2 Procedure

- i. After 7 days of cure, the propellant grain is removed from its mold and recorded its total length (24 mm) and diameter (25 mm).
- ii. Using a sharp blade, the grain is sliced into four equal circular sections. From each disk, six rectangular specimens (10mm x 6mm x 6mm) are cut.
- iii. Using a sharp blade, slice the grain into four equal circular sections, each approximately 6 mm thick.
- iv. From each 6 mm thick disk, cut six rectangular specimens measuring 10 mm × 6 mm × 6 mm, for a total of 24 samples per grain.
- v. Assign the label for each sample set, to ease of recognition for further experiments.
- vi. Confirm dimensions of a subset of samples with calipers to ensure uniformity within ±0.1 mm before testing.

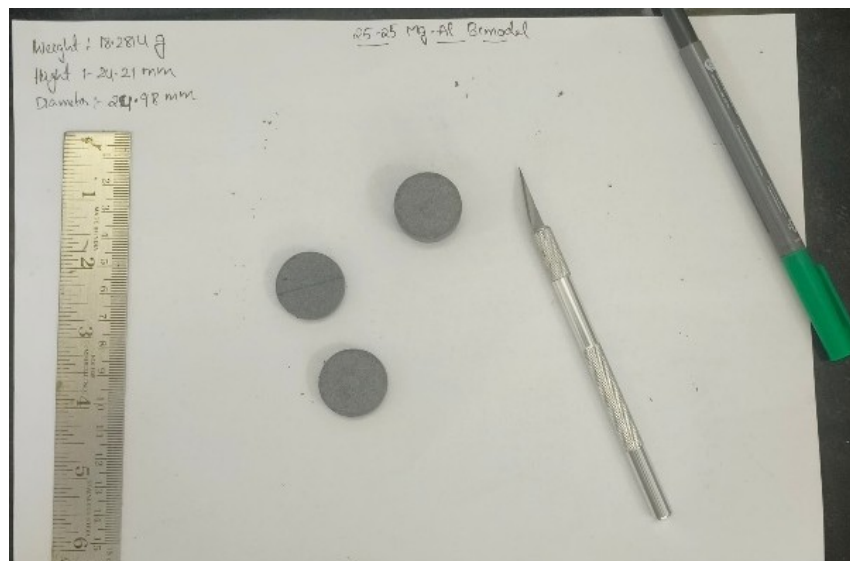


Figure 2.5: Cutting the propellant grain into uniform samples.

Chapter 3

Experimental Characterization

3.1 Bomb Calorimeter

3.1.1 Aim

To determine the heat of combustion of the propellant compositions.

3.1.2 Theory

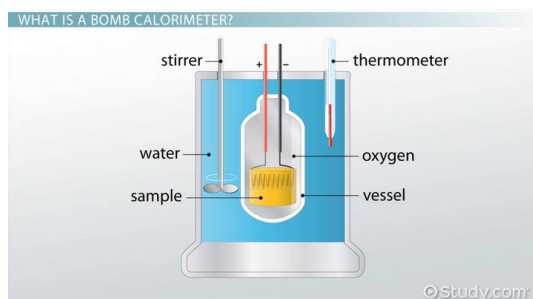
Determining the Heat of Reaction:

$$q_{rxn} = -q_{calorimeter}$$

$$q_{calorimeter} = q_{bomb} + q_{water}$$

The **water equivalent** of the calorimeter is the mass of water that would have the same **heat capacity** of the bomb calorimeter. The water equivalent is calibrated using a substance with a known calorific value, like Benzoic acid.

$$q_{calorimeter} = (\text{heat capacity of calorimeter}) \times \Delta T$$



(a) Bomb calorimeter components



(b) Semi-automatic bomb calorimeter setup

Figure 3.1: Bomb Calorimeter Setup

$$q_{\text{calorimeter}} = C_{\text{calorimeter}} \Delta T \quad (3.1)$$

$$q_{\text{rxn}} + q_{\text{nichrome}} + q_{\text{thread}} = q_{\text{calorimeter}} = C_{\text{calorimeter}} \Delta T \quad (3.2)$$

$$C_v m_{\text{sample}} + q_{\text{nichrome}} + q_{\text{thread}} = q_{\text{calorimeter}} = E \Delta T \quad (3.3)$$

$$C_v = \frac{E_{\text{water}} \Delta T - q_{\text{nichrome}} - q_{\text{cotton}}}{m_{\text{sample}}} \quad (3.4)$$

Where:

- C_v : Specific heat capacity at constant volume of the **sample** (J/g · K)
- E_{water} : Water equivalent of the calorimeter system (effective heat capacity in J/K)
- ΔT : Temperature change observed during the experiment (in C or K)
- q_{nichrome} : Heat released by the nichrome wire (J)
- q_{cotton} : Heat released by the combustion of cotton thread (J)
- m_{sample} : Mass of the sample (g)

This Bomb calorimeter setup is semi-automatic and once calibrated and it accounts for minimum variations in specific heat with temperature does the calculations and outputs the calorific value. Because solid propellants already have an oxidizer in them, we test the samples in a nitrogen atmosphere at 30bar pressure.

3.1.3 Procedure

1. 1g of sample is carefully weighed and tied with nichrome wire and attached to electrodes and put inside a crucible cleaned with acetone.
2. The chamber is sealed and pressurized to 30bar and slowly lowered into deionized water and this entire bucket is put inside the enclosure.
3. Electrodes are connected to a power source, a thermocouple is inserted, and a stirrer is installed.
4. When the temperature stabilizes, we close the fuse and the sample is ignited.
5. The machine calculates the rise in temperature and automatically gives the calorific value.

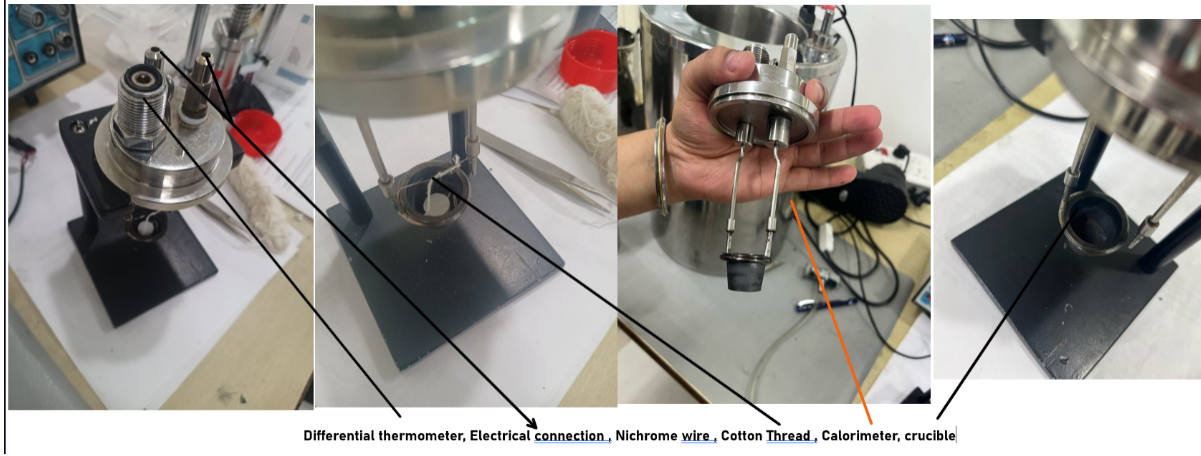


Figure 3.2: The key components: differential thermometer, electrical connections, Nichrome wire, cotton thread, calorimeter, and crucible.

COMPOSITION	TEST 1(cal/g)	TEST 2(cal/g)	TEST 3(cal/g)	TEST 4(cal/g)	TEST 5(cal/g)	Average Cal Value (cal/g)	STANDARD DEVIATION (cal/g)
60% Mg - Bimodal	874.58	1079.63	1284.56	1347.56	1404.98	1198.262	218.6967979
50% Al - Bimodal	642.19	765.22	665.28	-	-	690.8966667	65.39308399
30%-10% (Al-Mg) Bimodal	852.7	1730.32	2055.67	781.62	-	1355.0775	635.8389318
Nitrocellulose NCW	546.5	-	-	-	-	546.5	-
Equalylyptus oil white (Oz)	10304.14	10227.59	10336.95	9899.52	-	10192.05	200.3306189
Equalylyptus oil yellow (Oz)	11302.05	11077.87	10367.02	11807.84	-	11138.695	598.2256746

Figure 3.3: Calorific Values for different compositions

3.1.4 Observations

Table 3.1: Calorific Value Measurements of Bimodal Compositions

COMPOSITION	MEAN (kJ/kg/mol)	STANDARD DEVIATION
50% Al – Bimodal	3196.147	86.14
60% Mg – Bimodal	4922.295	147.669
30%-10% (Al–Mg) Bimodal	2413.983	72.419
40% Mg – Bimodal	3211.443	140.188
40%-10% (Al–Mg) Bimodal	4545.930	136.378

Inferences

- i. Higher metal content leads to higher energy: Mg-rich blends (60wt% Mg, $\approx 4922\text{ kJ/kg}$) outperform Al-rich ones (50wt% Al, $\approx 3196\text{ kJ/kg}$) due to higher Mg content and its greater oxidation enthalpy.
- ii. Mixed Al–Mg formulations exhibit a non-linear trend: moderate Mg additions (40–10% Al–Mg) yield higher energy output, while lower ratios (30–10% Al–Mg) result in lower calorific value.
- iii. Nitrocellulose (NCW of unknown composition) showed a calorific value (C_v) of 546.5 cal/g. According to literature, under a nitrogen atmosphere, the sample NCW-1342 has an average heat of explosion of $3.97 \pm 0.07\text{ kJ/g} \approx 945.6\text{ cal/g}$.

Justification for Variability in Calorific Values

$$C_v = \frac{E_{\text{water}} \Delta T - q_{\text{nichrome}} - q_{\text{cotton}}}{m_{\text{sample}}} \quad (3.5)$$

1. **Water equivalent is fixed in calibration.**
2. If any variations in temperature, quantity, or composition of water occur, they will alter the calorimeter equivalent, which is not accounted for by the instrument. Eg.: If you fill the bomb with more water than during calibration, the same released heat will produce a smaller temperature rise. This should be accounted for by increasing the water equivalent of the calorimeter, as a lower temperature rise corresponds to a higher water level.
3. **Mass should be precisely 1 g,** to ensure accurate calorific measurements.

Because the calorimeter calculates C_v for 1 g, any increase or decrease in the weight of the sample will cause the instrument to over- or underestimate the calorific value.

3.2 Burn Rate Experiment

Empirical Burning Rate Law (Saint Robert's Law):

The burning surface of a rocket propellant grain recedes in a direction perpendicular to this burning surface. The rate of regression, typically measured in inches per second (or mm per second), is termed *burning rate* (or *burn rate*).

The surface regression rate, r , is given by:

$$r = r_0 + aP_c^n \quad (3.6)$$

Where:

- P_c : local chamber pressure,
- a : burn rate coefficient (depends on propellant composition and temperature),
- n : pressure exponent (typically between 0.2 and 0.8 for composite propellants).

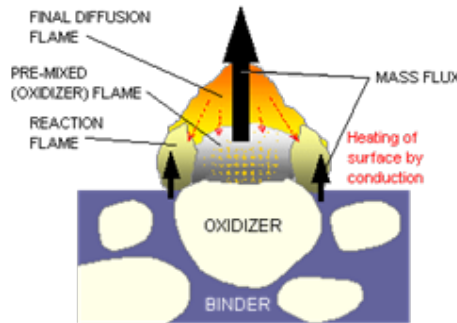


Figure 3.4: A schematic of the granular diffusion flame model for solid propellant combustion. It illustrates how heat is conducted from the flame back to the surface, sustaining the reaction.

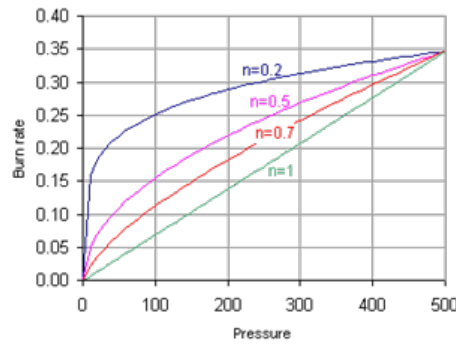


Figure 3.5: A graph showing the relationship between burn rate and pressure for various pressure exponents (n), as described by the burn rate law, $r = aP^n$.

To understand the burning rate mechanism, key processes include:

- Heating of the solid phase,
- Decomposition of oxidizer and binder (burn at different temperatures),
- Possible melting and vaporization,
- Vapor-phase mixing and reactions,
- Gas-phase combustion.

Factors influencing propellant burning rate:

- Combustion chamber pressure,
- Initial propellant temperature,
- Gas velocity parallel to the burning surface,
- Local static pressure,
- Motor acceleration and spin.

Burning rate is highly sensitive to the pressure exponent. High n values can dramatically increase the burning rate with small increases in pressure, potentially causing dangerous pressure escalation.

Experimental Setup

- A windowed strand burner is a high-pressure stainless-steel chamber designed to measure the linear burn rate of composite solid propellants by direct optical observation. Two quartz windows along the chamber wall provide optical access, while a nitrogen inlet and exhaust outlet allow the chamber to be pressurized, purged, and vented safely.
- Inside the chamber, the propellant sample—a slender “strand” cut to known dimensions—is mounted vertically on a ceramic pedestal. Its side faces (except the camera-facing front) are lightly greased with silicone to prevent lateral burning. Nichrome ignition wire is laid across the top of the strand and connected to a power source; when current passes through the wire, it heats and ignites the propellant.
- A high-speed video camera records the combustion through one window at 25 frames per second. A variable neutral-density filter attenuates flame brightness so the camera sensor isn’t saturated. Before each run, the camera is calibrated against a scale to establish pixel-to-millimeter conversion. The chamber is filled and purged with pure N₂ to eliminate oxygen and moisture, then pressurized to the desired test pressure.



Figure 3.6: Strand burner setup with camera and chamber

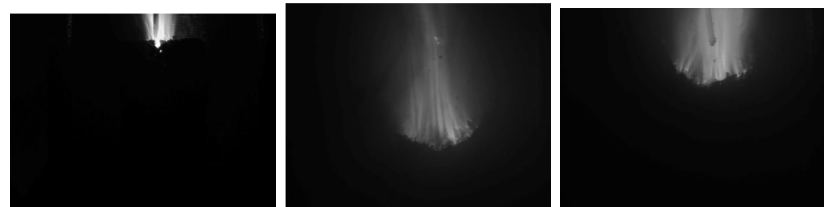


Figure 3.7: Sequential video frames showing flame front during strand burn

- Post-burn, each video frame is binarized in MATLAB: the bright (burned) region versus the dark (unburned) region. The flame front—the boundary line between bright and dark—is located on each frame. Because the time between frames is 40 ms, plotting flame-front displacement versus time yields a straight line whose slope is the strand’s burn rate. Each experiment is repeated twice for reproducibility.

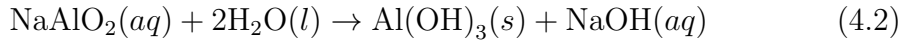
Chapter 4

Hydrolysis of Aluminum

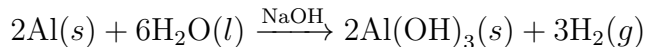
4.1 Introduction

Hydrolysis reactions of aluminum are utilized for hydrogen generation. Aluminum is an easily oxidized material. As soon as the bare aluminum surface enters into contact with air, it is oxidized. At neutral pH, this oxide is stable and insoluble, so hydrogen production stops.

In this study, NaOH is used as a catalyst to solve this problem. The Al hydrolysis reactions in a NaOH solution are the following:



The overall net reaction, where NaOH acts as a catalyst, can be summarized as:



Based on the stoichiometry of the reaction, the hydrolysis of 1 g of Al in an alkaline medium can produce 1245 ml of hydrogen (at NTP). The resultant product, Al(OH)_3 , is stable and non-corrosive. Moreover, this product is an important raw material for ceramic and allied industries, or it can be recycled back to aluminum via the Hall-Héroult process.

4.2 Al-Wire Feeding

Aluminum in the form of wire is used, and the feeding issues have been solved. The parameters of the hydrolysis, such as the solution temperature (25–80 °C), catalyst concentration (1–4 M NaOH), aluminum quantity, and aluminum wire diameter (0.6–1 mm), were optimized by adopting the response surface method (RSM) with laboratory-scale experiments. The aluminum wire feeding system is computer-controlled using a microcontroller-based code. Hydrogen production rates up to 350 ml/min have been accomplished.

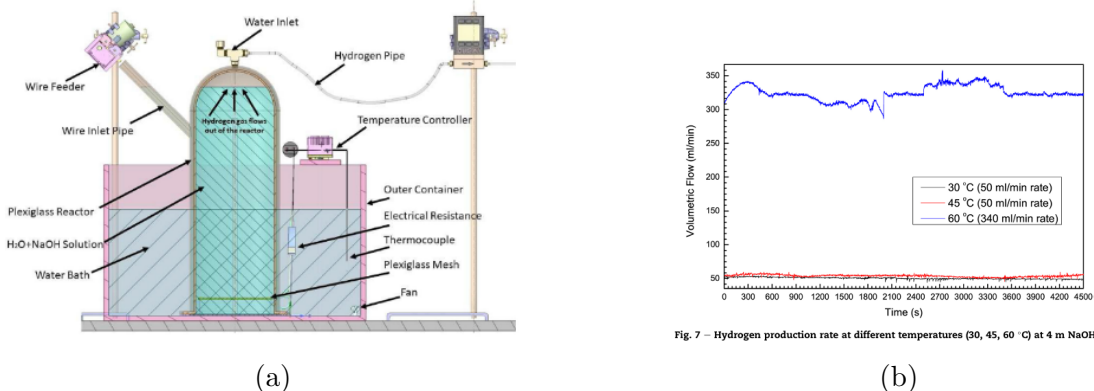


Figure 4.1: (a) Schematic of the hydrogen generation setup using Ni-Al alloy in NaOH solution. (b) Graph showing hydrogen evolution rate at different temperatures ,Peak occurs at 60 °C .

4.3 Al-Powder Injection

1. To increase the reaction rates, nano-sized aluminum particles are used, but this introduces an agglomeration problem. Additionally, the production of nano-aluminum is a costly process.
2. The maximum hydrogen production rate increases with increasing temperature and decreasing particle size, which is consistent with a surface reaction controlled by Arrhenius kinetics.

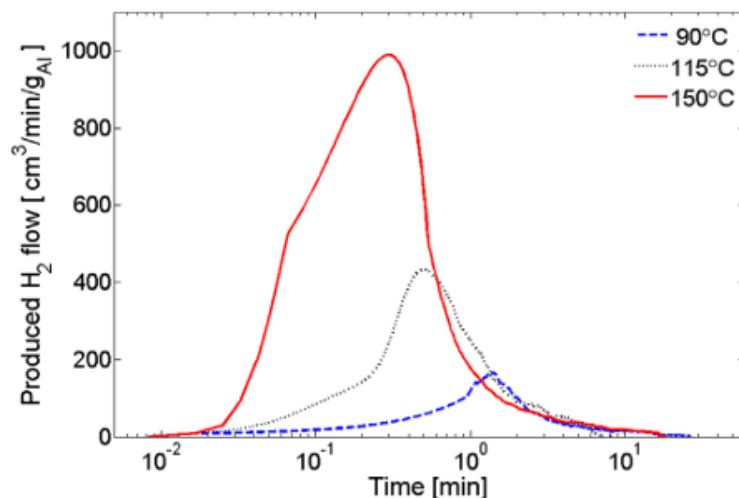


Fig. 5 – Produced hydrogen flow rate vs. time for experiments conducted with H-2 aluminum powder at different temperatures.

Figure 4.2: Hydrogen flow rate vs. time for H-2 aluminum powder at 90 °C, 115 °C, and 150 °C, showing increased production with temperature..

3. The finite hydrogen yield observed for larger particles and lower temperatures suggests that the reaction is inhibited after it progresses a certain depth into the

particles. This depth is termed the penetration thickness, which increases with temperature and is independent of particle size.

4.4 Micronized Powder vs. Wire Feed

- Yavor et al. (2013) investigated powders—nano (120 nm), “H-2” (6 μm), and “H-10” (13.8 μm)—and showed that smaller particles react faster and give a higher yield at the same temperature (e.g., at 70 °C, yield followed nano > 6 μm > 13.8 μm). They did not compare these results against a wire feed system.
- Nano particles yielded a reaction rate 4 times greater than that of 6 μm particles. In powder injection, hydrogen production continuously rose with an increase in water temperature, whereas the wire feeder system’s rate saturated at 60 °C.

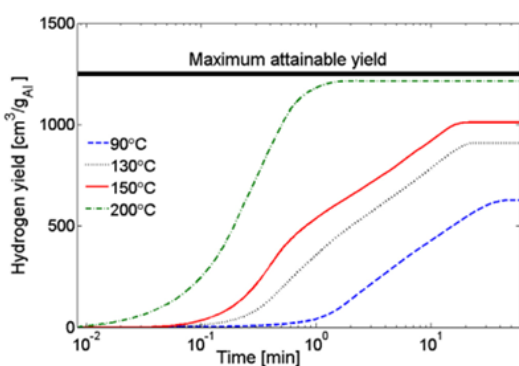


Fig. 6 – Hydrogen yield vs. time at various temperatures for experiments conducted with H-2 aluminum powder.

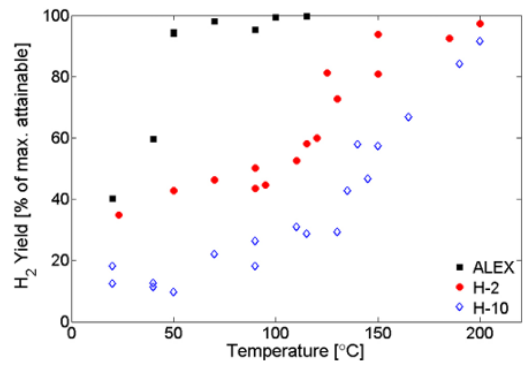


Fig. 11 – Hydrogen yield vs. reaction temperature for experiments conducted with ALEX, H-2 and H-10 aluminum powders.

(a) Hydrogen yield versus reaction time.

(b) Final hydrogen yield versus temperature.

Figure 4.3: Graphs illustrating hydrogen yield from aluminum powder hydrolysis.

4.4.1 Challenges

1. Achieving leakproof permanent connections.
2. Removal of the precipitate ($\text{Al}(\text{OH})_3$) formed during the reaction.
3. Designing a reliable Al powder injection setup.

4.5 Micronized Aluminum Injection Design

Current Injection Method: A basic syringe.

4.5.1 Objectives

1. Develop a leak-tight setup.
2. The setup must inject powder against high pressure and withstand high temperatures.

- No residual powder or slurry should remain inside the injection mechanism.

4.6 Proposed Solutions

Note on Materials: The use of metals like SS304L and SS316L should be avoided. Over time, the adsorption, diffusion, and accumulation of hydrogen atoms in the metallic lattice can cause hydrogen embrittlement.

1. Injection Molding Screw Setup

This concept involved using a power screw similar to those in injection molding machines. The idea was to manually turn the screw, causing it to translate and push powder into the reaction chamber against internal pressure.

Limitations: This idea was abandoned due to several issues. Aluminum particles are abrasive and would quickly wear out the screw and barrel. The flow of solid particles would be rough and improper. The required clearances would create pathways for hydrogen gas to escape.

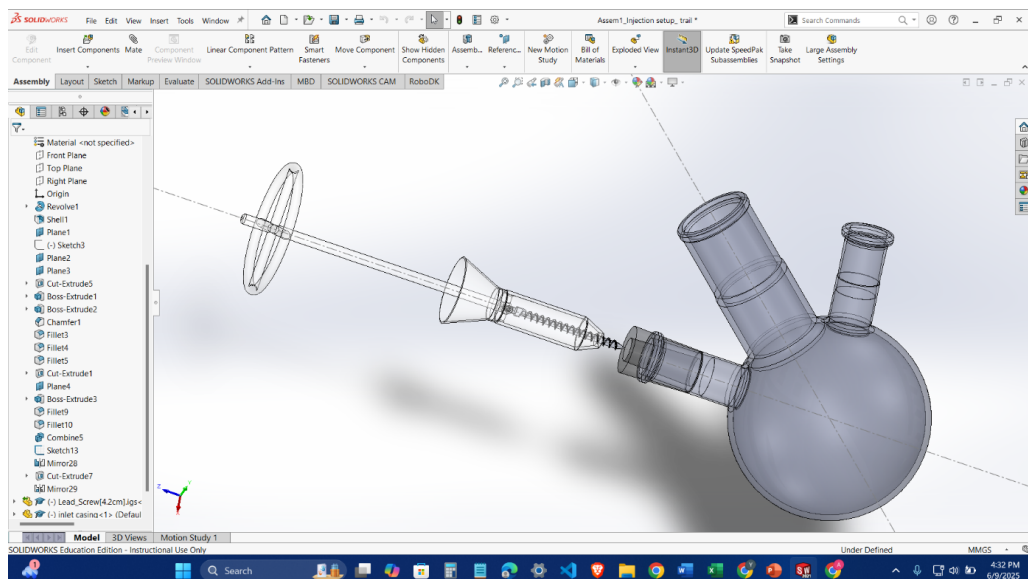


Figure 4.4: Exploded CAD view showing internal components of the pneumatic injection setup.

2. Tapered Nozzle Syringe Injection

This design features a tapered side port and a vertical riser to introduce a high-velocity air stream, which can fluidize and carry fine Al particles into the main vessel. A syringe-style plunger provides a fixed internal volume, allowing each stroke to deliver a reproducible powder dose. The pressure from the syringe could also help counter the reactor's internal pressure.

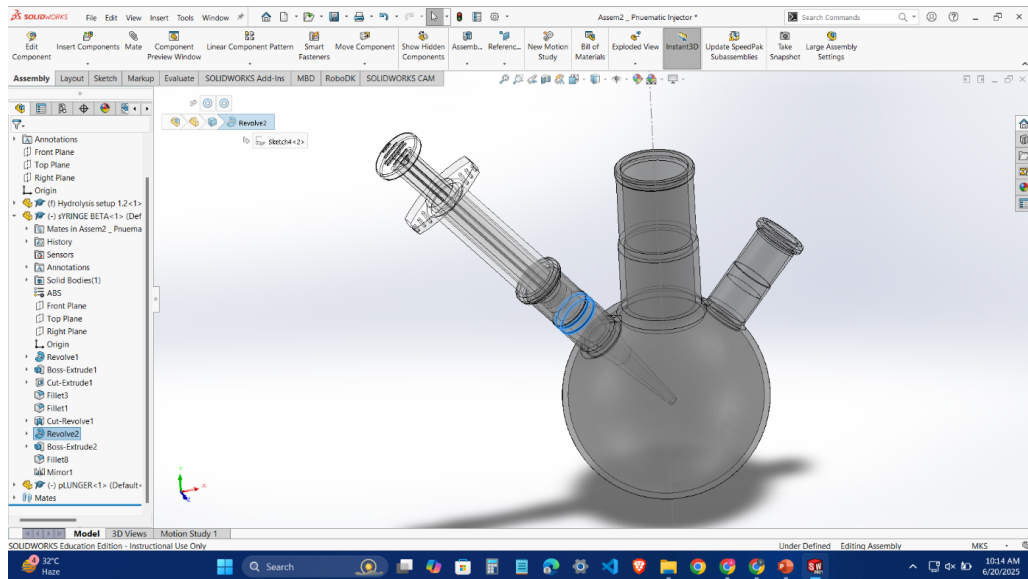


Figure 4.5: CAD model of a pneumatic injector assembly with syringe fully inserted into the reactor chamber.

Limitations: This idea was also abandoned. Abrasive Al particles can indent and damage plunger seals and O-rings. The high temperature would likely deform a 3D-printed syringe over multiple cycles, and finding a suitable plunger seal material is difficult. The powder is also prone to clogging near bends and constrictions, and clearances could still lead to leaks. The need arose for a simpler design with fewer moving surfaces in contact with the abrasive particles.

Chapter 5

Solid Rocket Motor Design Approach

5.1 Theory: Chamber Pressure with Propellant Burn and Water Injection

In a steady-state solid rocket motor with optional water injection (e.g., for cooling or shaping thrust profiles), the propellant's gas-generation rate must balance the mass flow through the nozzle and any injected liquid.

1. Propellant Gas Generation Rate

$$\dot{m}_g = \rho_p A_b \dot{r}, \quad \dot{r} = a P_c^n \quad [\text{m/s}]$$

ρ_p Propellant density (kg/m^3)

A_b Burning surface area (m^2)

a, n Empirical burn-rate law constants

\dot{r} Instantaneous regression rate (m/s)

P_c Chamber pressure (Pa)

2. Mass Flow Out Through Nozzle Throat

$$\dot{m}_{\text{throat}} = \frac{P_c A_t}{C^*} \quad [\text{kg/s}]$$

A_t Nozzle throat area (m^2)

C^* Characteristic velocity (m/s)

3. Water Injection Rate (through orifice)

$$\dot{m}_w = C_d A_{\text{inj}} \sqrt{2 \rho_w \Delta P} \quad [\text{kg/s}]$$

C_d Discharge coefficient (dimensionless)

A_{inj} Injector orifice area (m^2)

ρ_w Water density (kg/m^3)

ΔP Pressure drop across injector (Pa)

4. Overall Mass Balance

$$\dot{m}_g = \dot{m}_{\text{throat}} + \dot{m}_w \implies \rho_p A_b (a P_c^n) = \frac{P_c A_t}{C^*} + C_d A_{\text{inj}} \sqrt{2 \rho_w \Delta P}$$

5. Solving for Chamber Pressure

$$\rho_p A_b a P_c^n - \frac{A_t}{C^*} P_c - C_d A_{\text{inj}} \sqrt{2 \rho_w \Delta P} = 0$$

This is a transcendental equation in P_c and must be solved numerically (e.g., using Newton–Raphson or root-finding algorithms).

Special Case (No Water Injection):

$$\text{If } \dot{m}_w = 0, \quad P_c = \left(\frac{\rho_p A_b a C^*}{A_t} \right)^{\frac{1}{1-n}}$$

5.2 Open Motor Simulation

Open Motor is an open-source, Python-based internal-ballistics simulator and GUI for designing and analyzing solid and hybrid rocket motors. It allows you to define grain geometries, propellant burn-rate laws, and nozzle parameters to predict thrust, chamber pressure, and specific impulse. This tool was used to connect the experimental data with theoretical performance predictions.

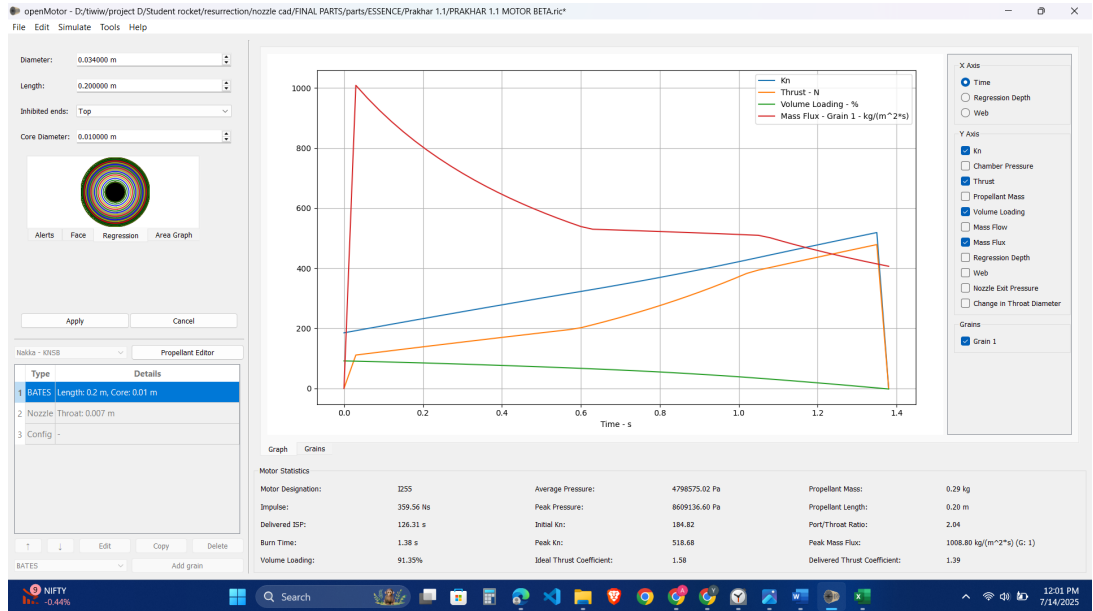


Figure 5.2: OpenMotor GUI for rocket motor simulation.

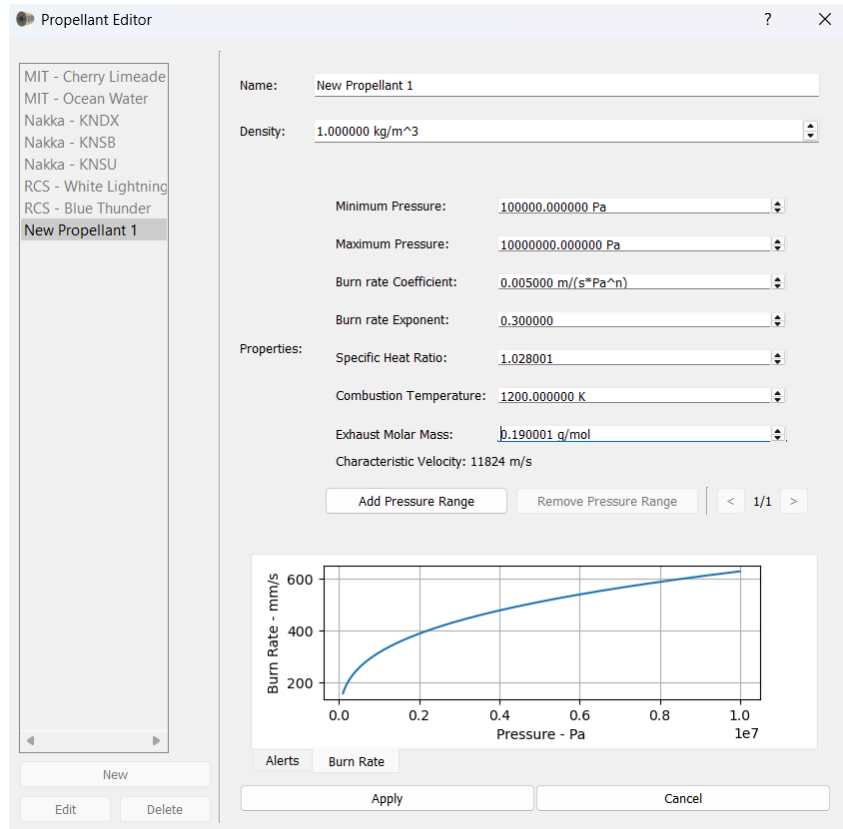


Figure 5.3: Defining propellant properties and grain geometry in OpenMotor.

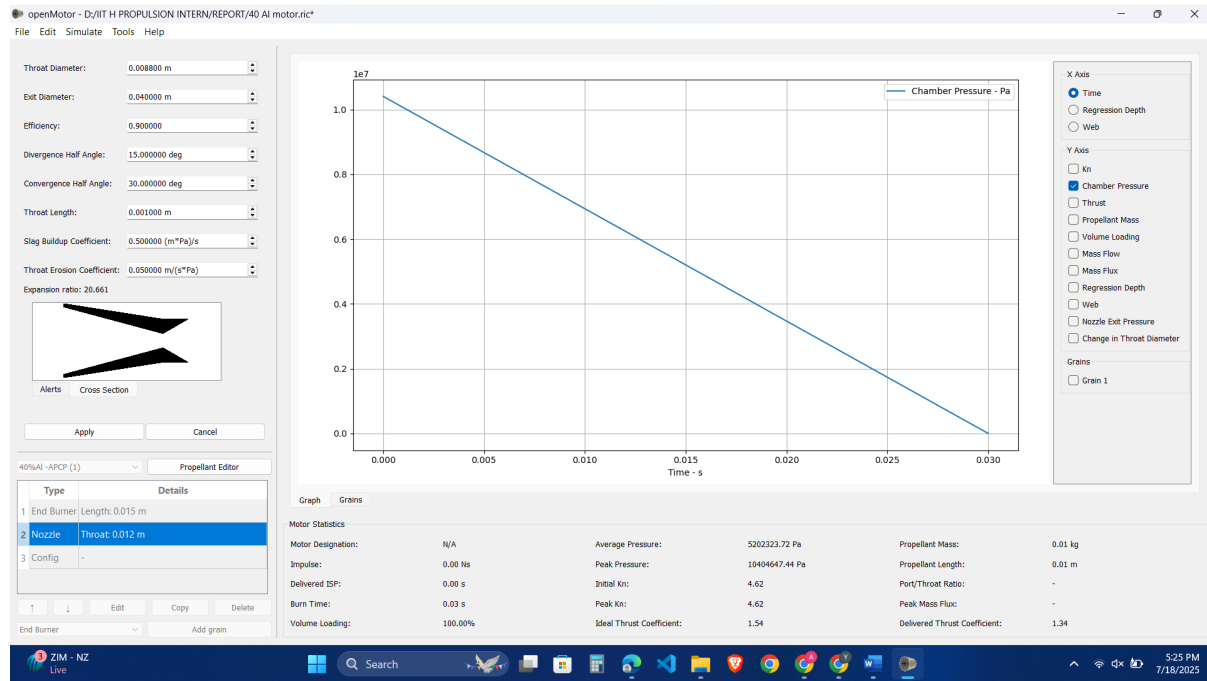


Figure 5.4: Nozzle properties inside OpenMotor.

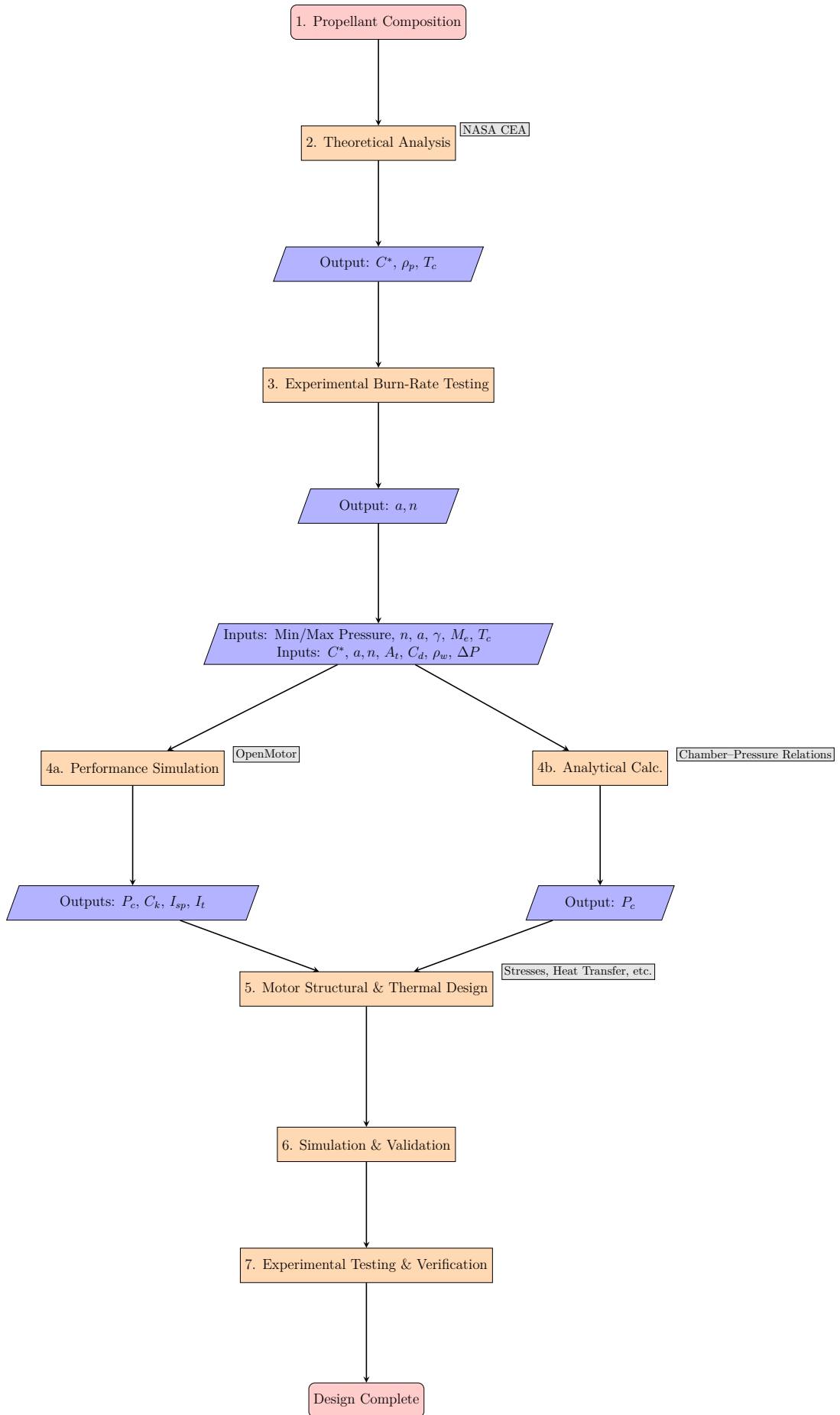


Figure 5.1: Solid Rocket Motor Design Approach

Chapter 6

Hydro-Reactive Fuel Test Stand

6.1 Design of Test Chamber

A metal-water-reaction-based, water-breathing jet propulsion system that essentially uses highly metalized (Al, Mg or B) fuel-rich propellant in a dual combustion chamber with surrounding ambient water as the oxidizer. We aim to develop a test setup to replicate this phenomenon.

The functional requirements are as follows , Test bed - high pressure water injection system, split thrust chamber, variable primary and secondary nozzles,high temperature and pressure transducers, As discussed in the introduction, higher metal content increases energy density but, it requires excess of oxidizer to completely react and get stabilized, when there is abundance of oxidizer we can have metal rich propellants, which can undergo primary combustion initially and the unburnt metal rich substances enter secondary combustion where they react with water and release more energy. Overall, a greater number of species undergo redox reactions, contributing to a higher release of energy.

6.1.1 Design Requirements

- A primary chamber (30 bar pressure, 2000K Temperature).
- A secondary chamber (30 bar pressure, 2000K Temperature).
- High pressure water inlets at +63,-63 and 90 degrees with multiple configurations.
- Nozzles for primary and secondary chambers.
- Ports for pressure and temperature transducers.
- A test bed with 3 Degrees of Freedom (DOF).

6.1.2 Materials used:

AISI 1080, Graphite, O-rings, Gaskets , M6x1.25 Nuts ,Bolts and washers ,etc.

6.2 The Mass Ejection Efficiency Test Bed:

6.2.1 The Prelimininny design requirements

$P_{in}=130\text{bar}$, Inlet N2 gas at 130bar , graphite nozzle , variable chuck for holding samples of different diameters, linear bearings , load cell.

6.2.2 General Stresses in Pressurized Cylinders

For a cylinder with an inside radius r_i , outside radius r_o , internal pressure p_i , and external pressure p_o , the tangential and radial stresses at any radius r are given by Lamé's equations:

$$\sigma_t = \frac{p_i r_i^2 - p_o r_o^2}{r_o^2 - r_i^2} + \frac{(p_i - p_o)r_i^2 r_o^2}{r^2(r_o^2 - r_i^2)} \quad (6.1)$$

$$\sigma_r = \frac{p_i r_i^2 - p_o r_o^2}{r_o^2 - r_i^2} - \frac{(p_i - p_o)r_i^2 r_o^2}{r^2(r_o^2 - r_i^2)} \quad (6.2)$$

The tangential and radial stresses are orthogonal and can be modeled as principal stresses on a stress element.

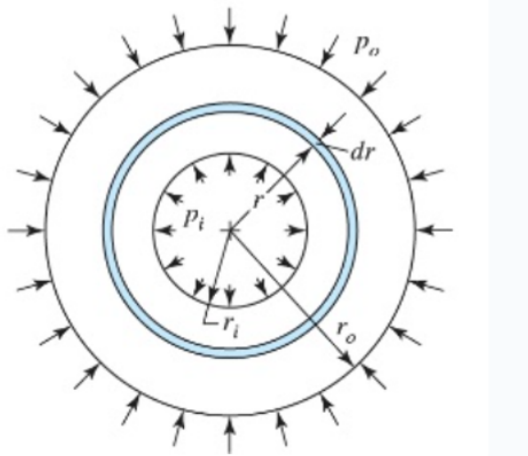


Figure 6.1: Stresses in a pressurized cylinder.

6.2.3 Maximum Stresses with Internal Pressure Only

To evaluate the maximum stresses, which occur at the inside radius ($r = r_i$), we consider the case of internal pressure only ($p_o = 0$). The equations simplify to:

$$(\sigma_t)_{\max} = p_i \frac{r_o^2 + r_i^2}{r_o^2 - r_i^2} \quad (6.3)$$

$$(\sigma_r)_{\max} = -p_i \quad (6.4)$$

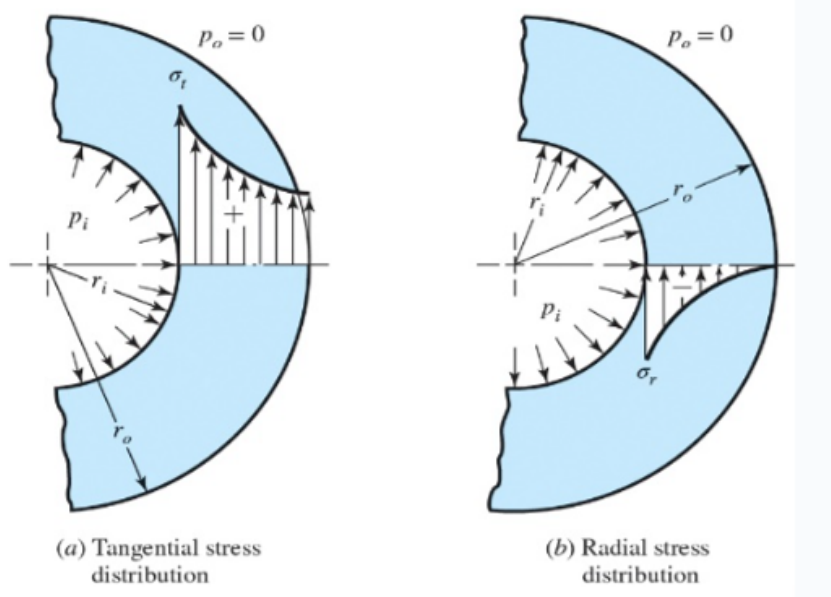


Figure 6.2: Tangential and radial stress distribution for internal pressure only.

6.2.4 Longitudinal Stress in Closed-End Cylinders

If the ends of the cylinder are closed, the internal pressure creates forces on the ends, leading to a longitudinal stress (σ_l) in the cylinder walls, given by:

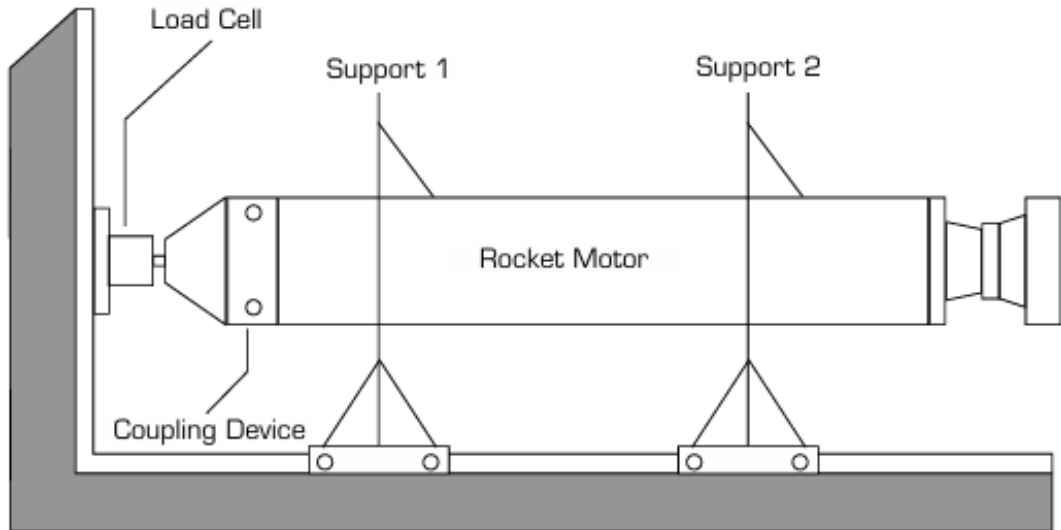
$$\sigma_l = \frac{p_i r_i^2}{r_o^2 - r_i^2} \quad (6.5)$$

Table 6.1: Calculation of Hoop, Radial, and Longitudinal Stresses (σ_y (AISI 1080) = 400MPa)

Primary Chamber									
Ri (m)	Ro (m)	r (m)	Pi (Pa)	Po (Pa)	t (m)	σ_t (MPa)	σ_r (MPa)	σ_l (MPa)	Design Factor
0.030	0.035	0.030	14 184 397.160	101 317.120	0.005	-141.844	919.804	392.799	0.435
0.030	0.045	0.030	14 184 397.160	101 317.120	0.015	-141.844	365.147	113.475	1.095
0.030	0.055	0.030	14 184 397.160	101 317.120	0.025	-141.844	259.110	60.075	1.544
0.030	0.065	0.030	14 184 397.160	101 317.120	0.035	-141.844	216.057	38.394	1.851
0.030	0.075	0.030	14 184 397.160	101 317.120	0.045	-141.844	193.467	27.018	2.068
0.020	0.039	0.020	3 039 513.680	101 317.120	0.019	-30.395	49.337	10.846	8.107

Secondary Chamber									
Ro (m)	r (m)	Pi (Pa)	Po (Pa)	t (m)	σ_t (MPa)	σ_r (MPa)	σ_l (MPa)	Design Factor	
0.045	0.055	0.045	3 039 513.680	101 317.120	0.010	-30.395	147.366	61.550	2.714
0.045	0.060	1.045	3 039 513.680	101 317.120	0.015	36.639	36.888	39.079	10.844
0.045	0.065	2.045	3 039 513.680	101 317.120	0.020	26.004	26.059	27.977	15.350

For the Primary Chamber A design factor of approximately 2 is achieved at a thickness of 0.045 m, and for the secondary chamber, a design factor of 2.714 is achieved at a thickness of 0.010 m.



Source: Elaborated by the authors.

Figure 1. Typical set up of a SRM firing test.

Figure 6.3: A typical setup for a Solid Rocket Motor (SRM) firing test.

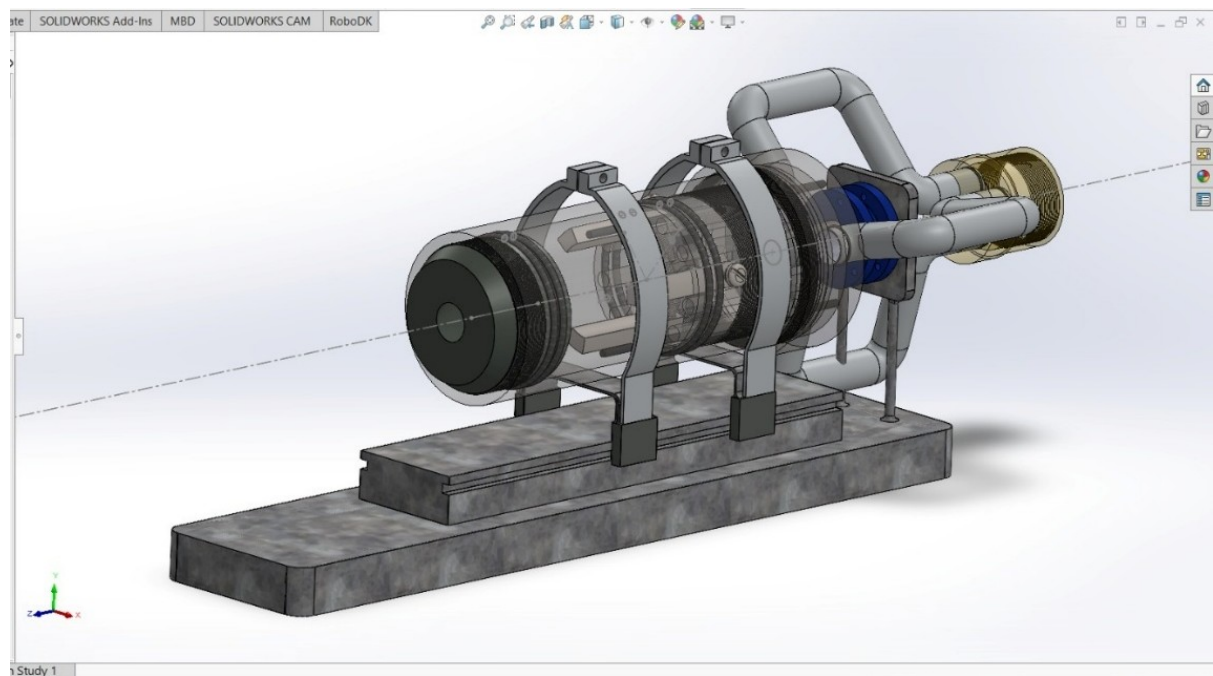


Figure 6.4: A detailed CAD model of the SRM assembly, showing internal components and support structures.

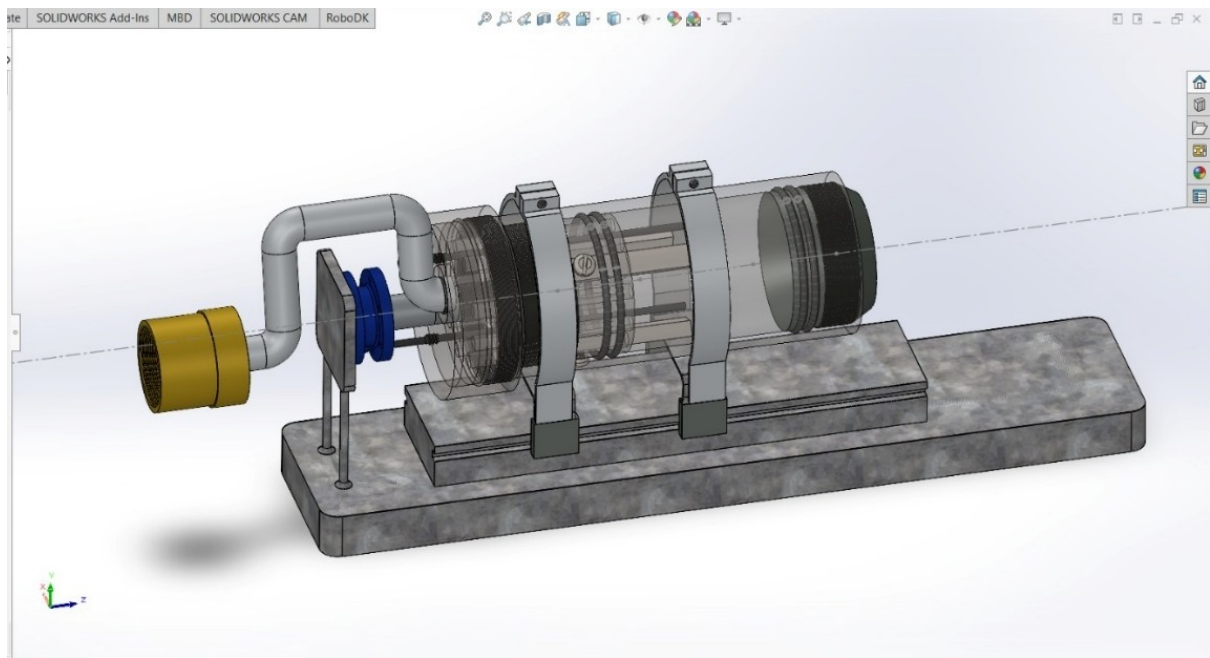


Figure 6.5: An alternative CAD view, highlighting the nozzle section and external connections.

6.3 The Test Bed Design

6.3.1 Design Requirements

The test bed was designed with the following key requirements:

1. Aligning the load cell axis with the test chamber.
2. A test bed with 3 Degrees of Freedom (DOF) for adjusting in length (x), height (y), and lateral position (z).
3. The ability to support the weight of the test chamber and slide smoothly.
4. Ease of making different configurations with the primary, secondary, and nozzle sections.

6.3.2 Components and Construction

The test bed is constructed using standard components to ensure modularity and ease of assembly. The primary components are shown below.

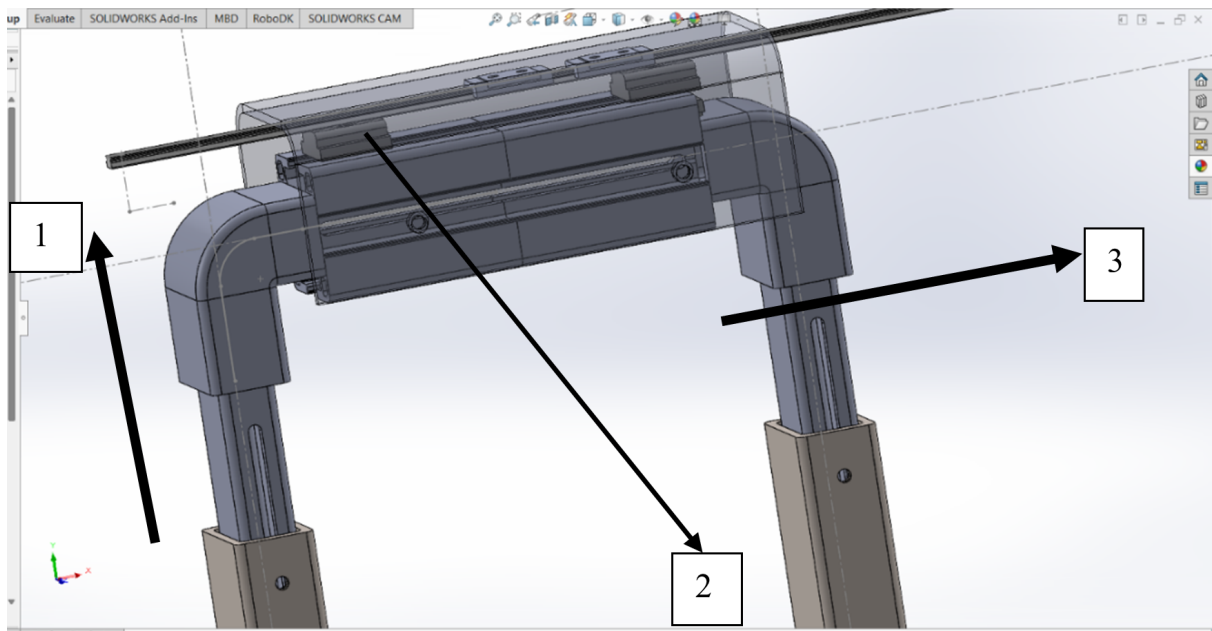


Figure 6.6: CAD views illustrating the 3-DOF adjustment capabilities of the test bed, including height (y-axis) [1], lateral position (z-axis)[3], and miniature linear guides[2] for smooth and precise movement

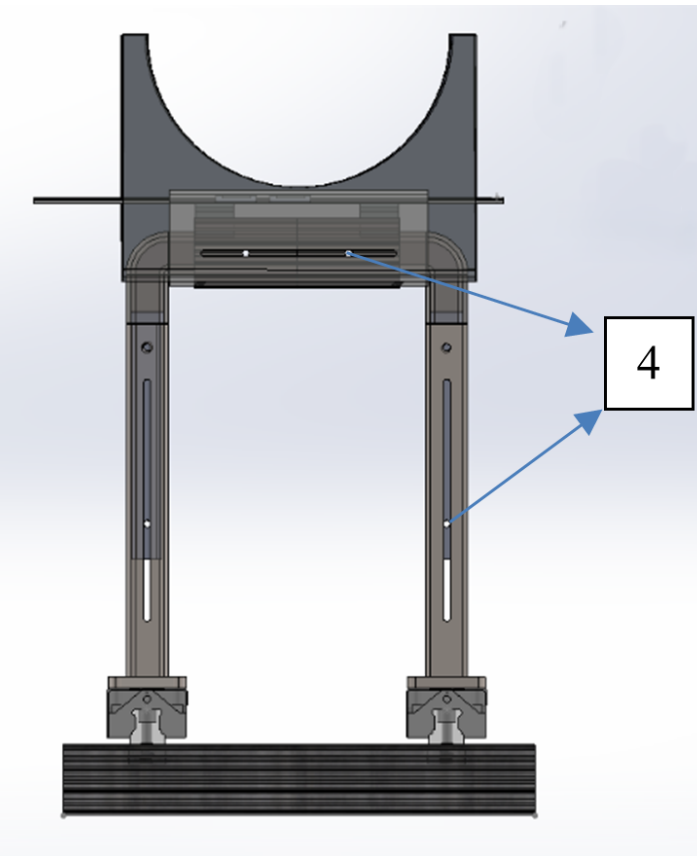


Figure 6.7: Slots for tuning positioning in x y and z,upon reaching the desired height an M6 bolt can be used to held the position .

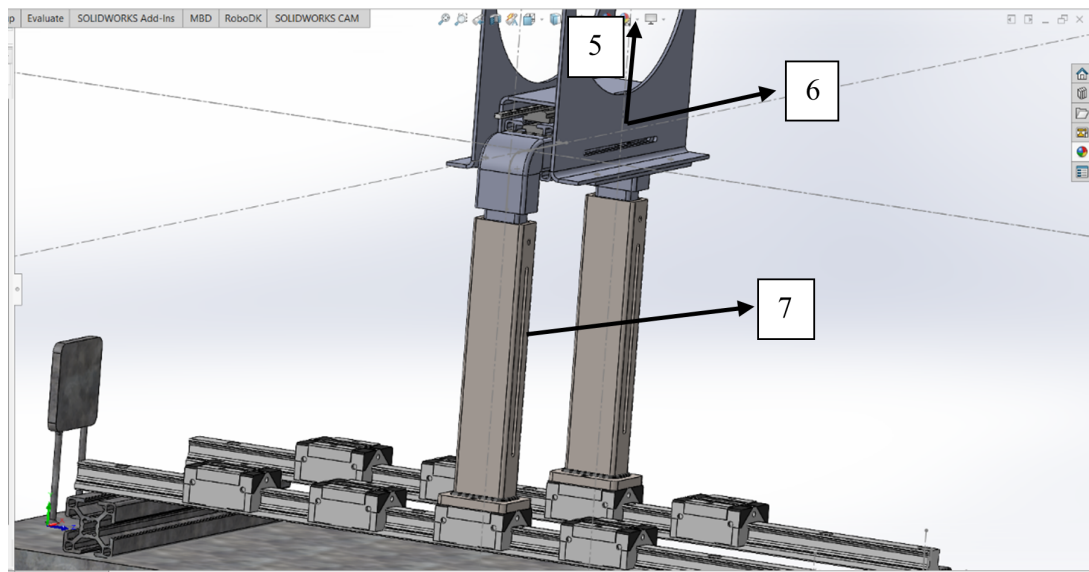


Figure 6.8: DOF along y (5), DOF along z (6), and a slot to adjust and hold position along y direction (7).

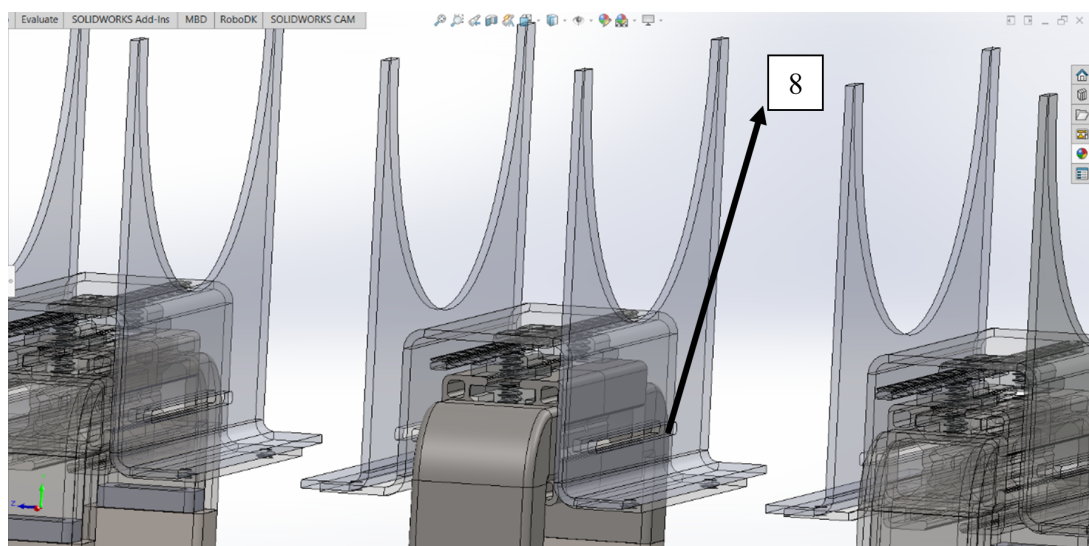


Figure 6.9: Slot to adjust the displacement along z (8)

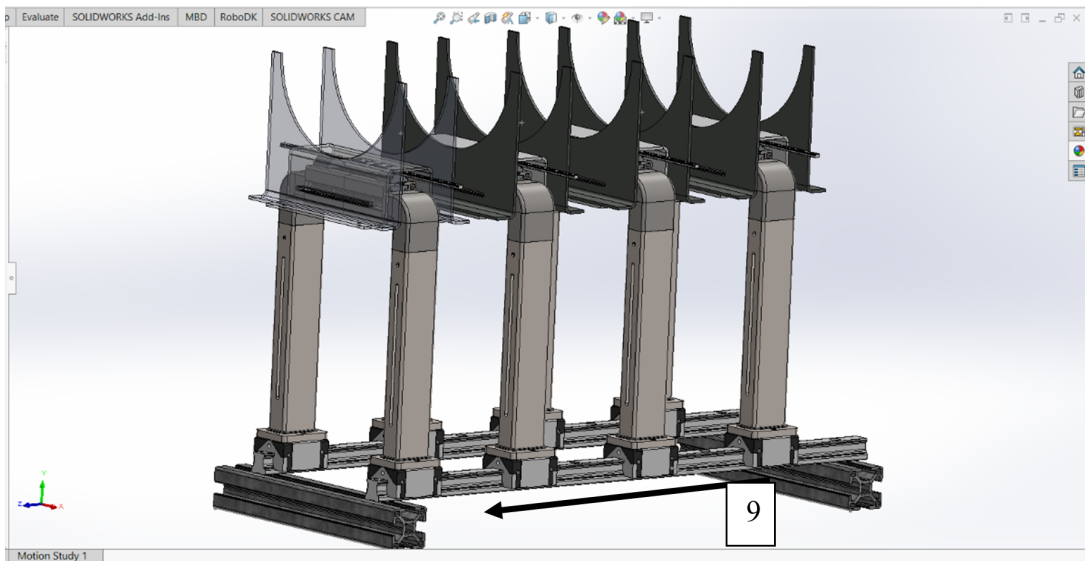


Figure 6.10: The complete test bed assembly, highlighting the linear guide rail (9) which allows for longitudinal adjustment along the x-axis.

6.3.3 Component Specifications

This section details the specific components selected for the construction of the test bed, including linear guides, the support frame, support legs, and fasteners.

Linear Guides

High-capacity profile rail linear guides are used for the primary sliding mechanism along the x-axis. The selected ARC series features an alloy steel bearing and can handle significant loads.

Products - ARC series Profile Rail Linear Guide	
	Product Overview
	Model Number: ARC series
	Bearing Type: Profile Rail Linear Guide
	Key Feature: Standard Profile Rail Linear Guides
	Sizes: 15, 20, 25, 30, 35, 45, 55
	Number of Rows: 4 rows of re-circulating balls
	Load Capacity: From 9.7 to 112.8 kN
	Material: Alloy Steel bearing, rail & balls
	Temp Range: - 40 F to +176 F (- 40 C to +80C)
	Delivery: Stock
Part Number Load Capacity Accuracy Specs Preload Specs Complete Profile Rail Catalog	

Figure 6.11: Product overview for the ARC series profile rail linear guides, showing key features such as a load capacity of 9.7 to 112.8 kN and construction from alloy steel.

Base Support Frame

The structural frame of the test bed is built from a standard, modular aluminum extrusion, allowing for easy assembly and modification.

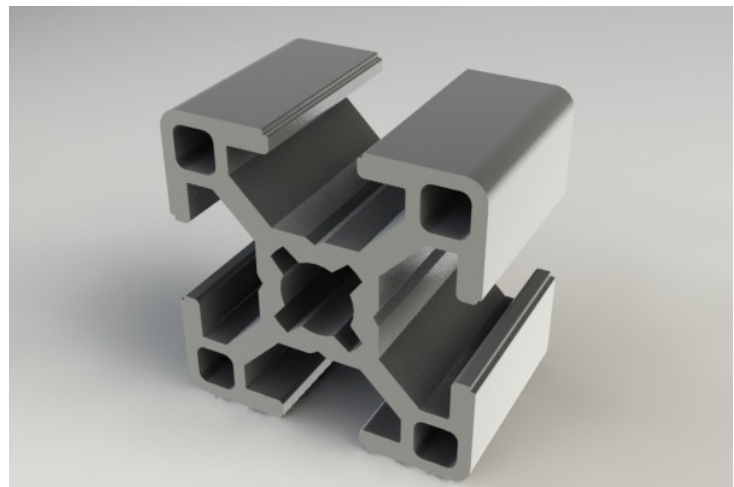


Figure 6.12: A 30-30 series aluminum T-slot extrusion is used for the base support frame.

Support Legs

The vertical supports are custom-designed to hold the chamber cradles and provide height adjustment.

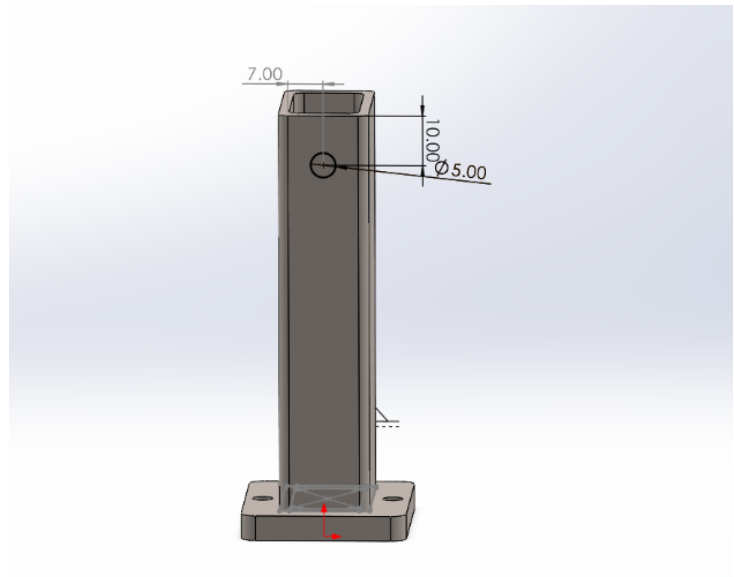


Figure 6.13: CAD model of a support leg, designed to be machined from AISI 1080 steel.

T-Slot Nuts

Standard T-slot nuts are used to secure components to the aluminum T-slot frame. The NTFS10(B=16) size is selected for this 30x30 extrusion.

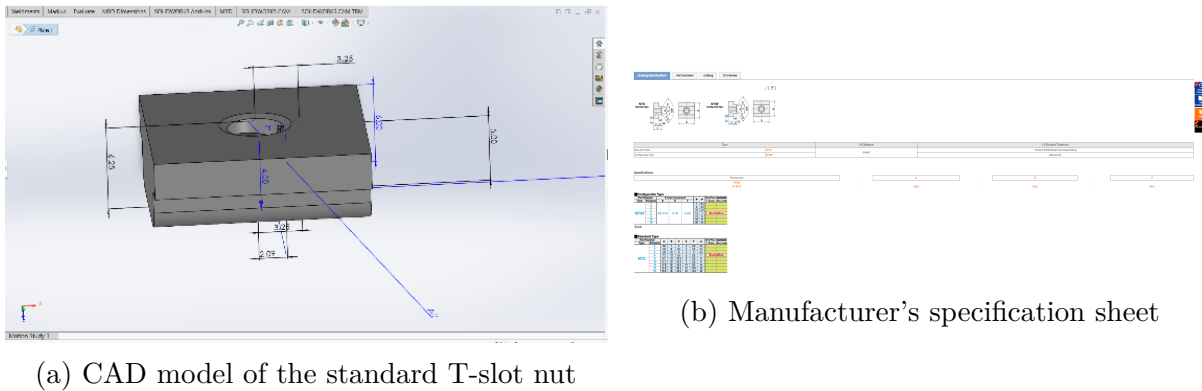


Figure 6.14: CAD model and specifications for the selected NTS series T-slot nuts.

Component List Sources

- **Linear Guides:** Key components for smooth x-axis motion. Resource links include:
 - <https://in.misumi-ec.com/vona2/detail/110310552239/>
 - <https://in.misumi-ec.com/vona2/detail/110310458729/>
 - <https://www.lintechmotion.com/products2.cfm?ModelNo=4&t=Group12>
- **Structural Frame:** 30-30 Aluminum T-slot extrusion.
 - <https://in.misumi-ec.com/vona2/detail/110302686450/t>
- **Fasteners:** T-slot nuts, for securing components to the frame.
 - <https://in.misumi-ec.com/vona2/detail/110310154259/t>

6.4 Design of the Test Chamber

The following section outlines the design requirements and an initial conceptual design for the test chamber assembly.

Design Requirements

The design was guided by the following key requirements:

1. A primary chamber designed for 30 bar pressure and 2000K Temperature.
2. A secondary chamber also designed for 30 bar pressure and 2000K Temperature.
3. High-pressure water inlets at 63 degrees, with configurations for 63, 27, and 90-degree injection.
4. A nozzle in the primary chamber to improve the mass ejection efficiency.

5. A secondary chamber nozzle to harness thrust from high-pressure gas.
6. Integration of pressure and temperature transducers.
7. A part for a variable nozzle exit diameter.
8. A test bed with 3-DOF (adjusting in length(x), height(y), and along (z)).
9. A test bed with easy accessibility and the freedom to have different configurations with or without the secondary chamber.

6.4.1 Conceptual Design 1: Threaded Joint Assembly

An initial conceptual design was developed based from locking mechanism of a Bomb calorimeter, chosen for its potential for easy assembly and disassembly. The core mechanism involved a large threaded nut. As the nut is rotated, it pulls the primary and secondary chambers together, compressing O-rings to provide a complete seal.

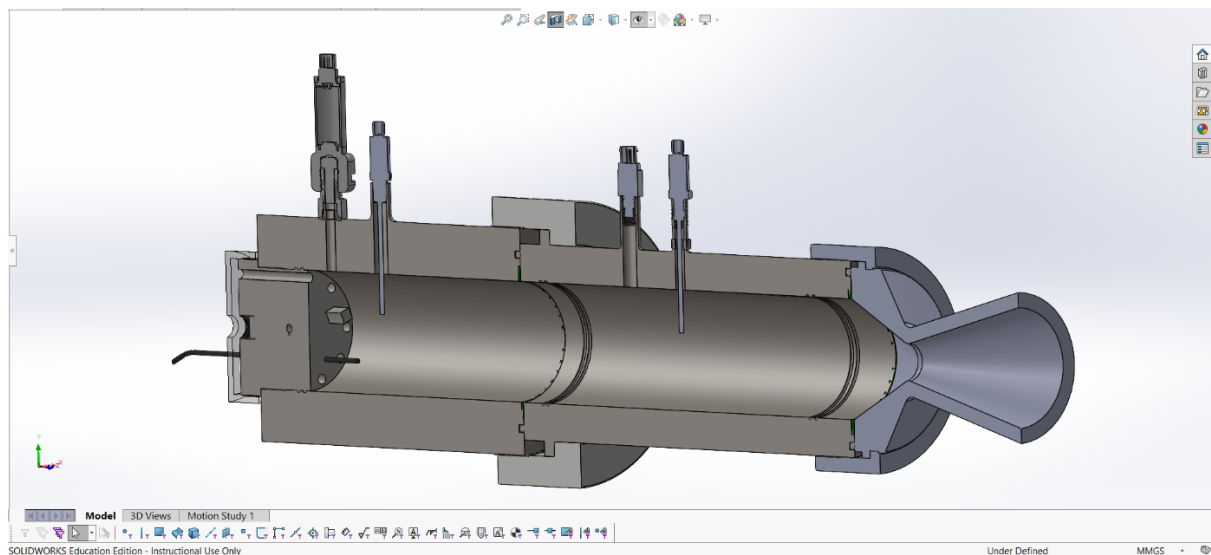


Figure 6.15: Cross-section of the conceptual threaded design. As the main nut is tightened, the chambers are pulled together, compressing the O-rings to create a seal.

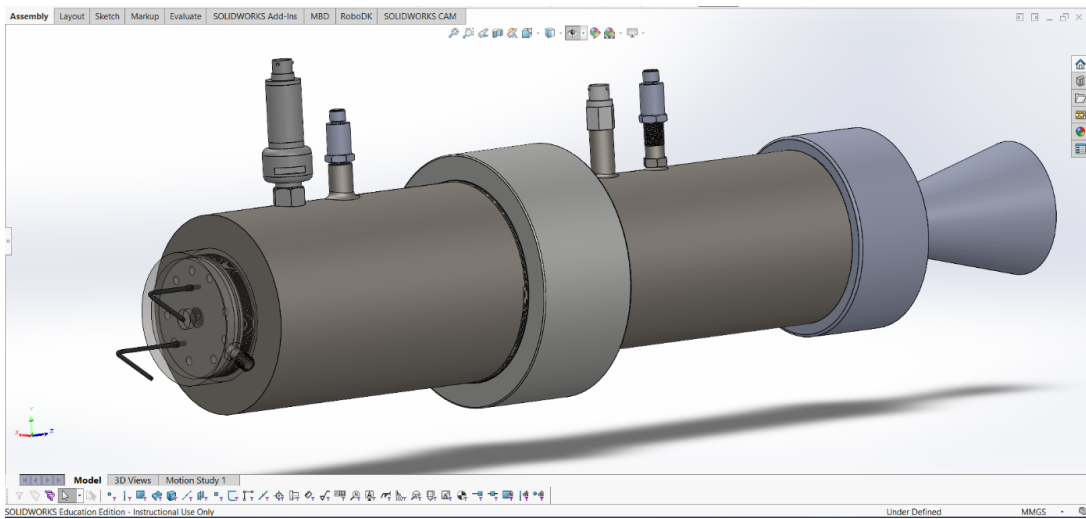


Figure 6.16: An isometric view of the thread joint test chamber assembly.

Limitations and Rejection of Concept

This concept was ultimately scrapped due to significant limitations. The large threaded joint would be prone to loosening from vibrations, a common issue in solid rocket motors. Furthermore, the threads could undergo plastic deformation and become unusable after a few thermal stress cycles. So this idea was scrapped.

6.4.2 Conceptual Design 2: Flange Joint

After rejecting the initial threaded joint concept due to its limitations, a universally used flange design is implemented. Flanges are widely used in high-pressure and high-temperature systems and offers significant advantages.

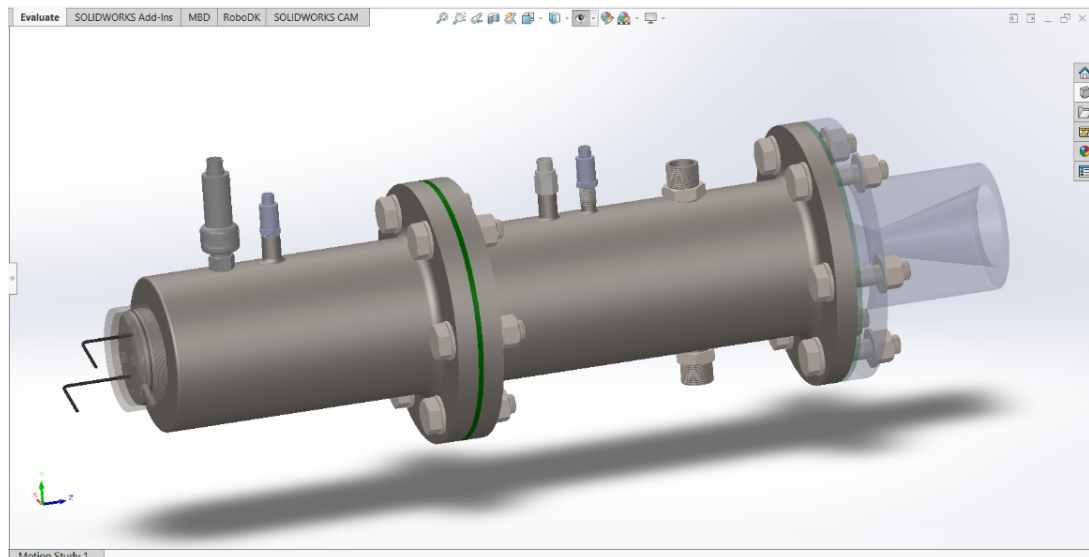


Figure 6.17: CAD model of the test chamber assembly using bolted flange joints between the primary chamber, secondary chamber, and nozzle section.

6.5 Madras Test Bed Drawings and Design

This section details the design of the Madras Test Bed, which was developed by adapting and modifying existing research.

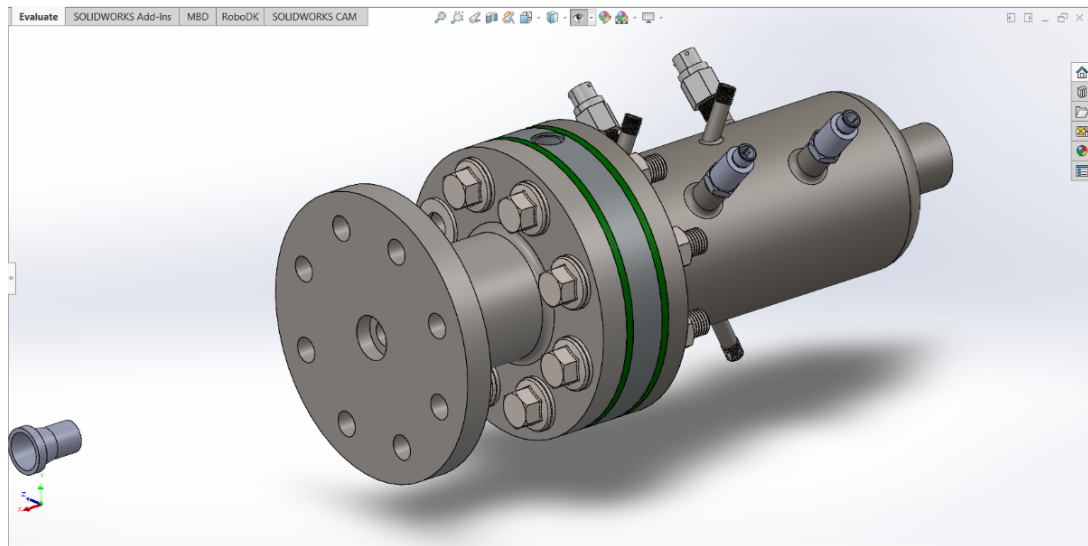


Figure 6.18: Isometric view of the Madras Test Bed CAD assembly.

6.5.1 Design Inspiration and Modifications

The drawings for the test setup were inspired by the paper "Investigation on Hydro-reactive Fuel Powered Water-breathing Jet Propulsion for High-speed Underwater Vehicles". The design was then further modified to incorporate a variable setup.

The water injection angle of 63 degrees and the placement of the injectors were taken from the paper "Effect of primary water injection angle on thermal propulsion performance of a water ramjet engine". The placement of temperature and pressure transducers was chosen to reduce stress concentration factors.

THRUST CHAMBER

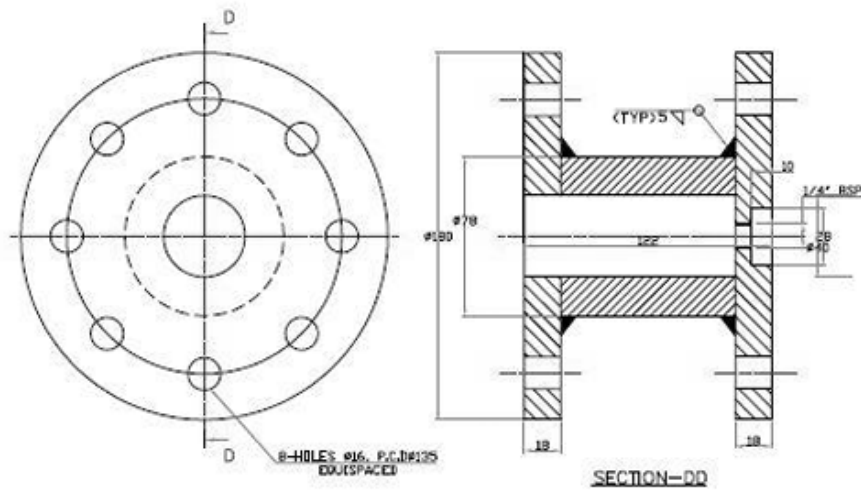


Figure A.11 Thrust chamber: Primary chamber.

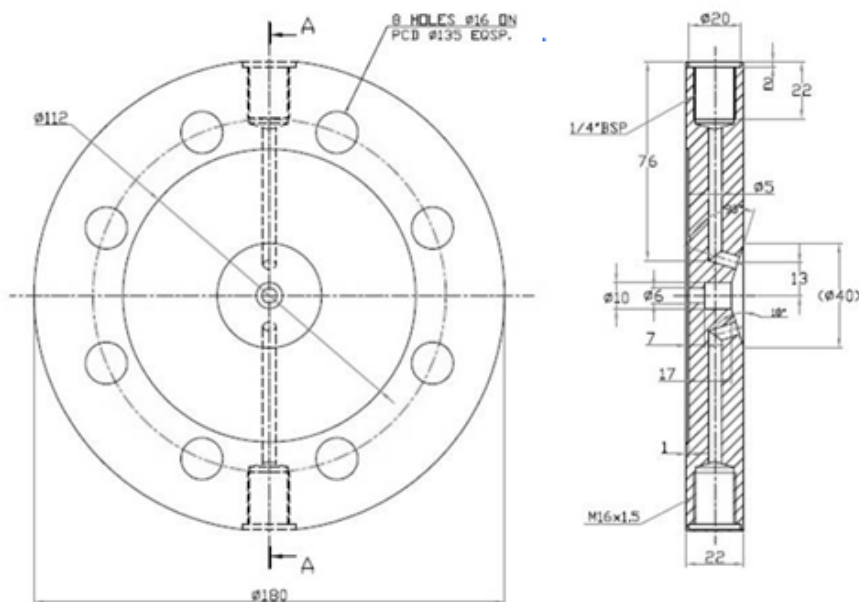


Figure A.12 Thrust chamber: Intermediate plate.

Figure 6.19: Technical drawings of the thrust chamber and intermediate plate that was referenced.

6.5.2 Water Injection System

The design incorporates both axial (α) and tangential (β) water injection capabilities to study their effects on performance. A schematic of this is shown below, along with the CAD implementation.

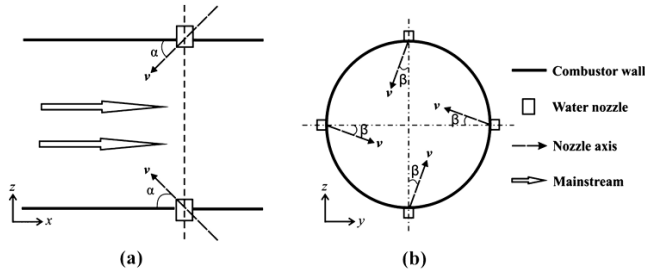
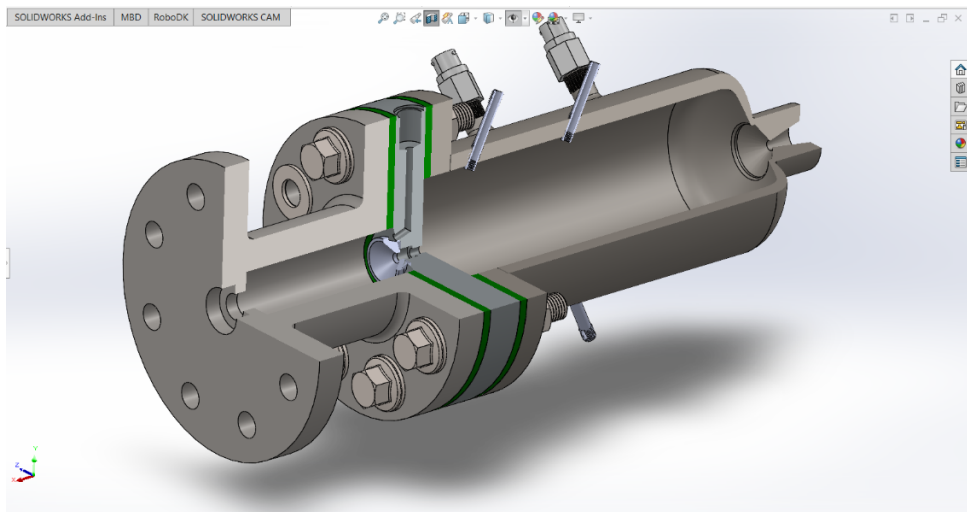


Fig. 3. Schematic diagram of axial angle and tangential angle of primary water injection in a WRE. (a) Axial angle of primary water injection; (b) Tangential angle of primary water injection.

(a) Schematic of axial angle (α) and tangential angle (β) of primary water injection.



(b) CAD cross-section showing the internal water injection nozzle.

Figure 6.20: Water injection system schematic and CAD implementation.

6.5.3 Performance Analysis from Literature

The design choices were informed by performance data found in the literature, which shows how injection angles affect key metrics like specific impulse (I_{sp}), outlet velocity (V_{out}), and outlet pressure (P_{out}).

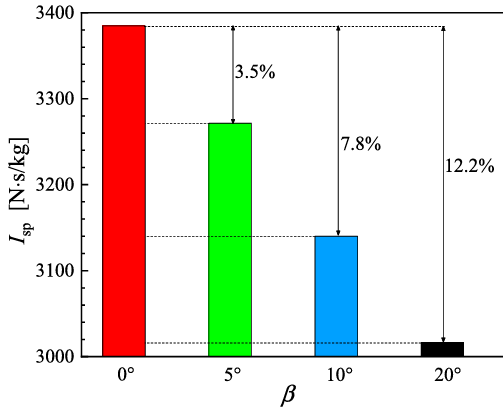


Fig. 22. Comparison of specific impulse I_{sp} for four different tangential injection angles β , $R_{w,f1} = 0.4$ and $R_{w,f2} = 1.6$.

(a) Specific impulse (I_{sp}) decreases as the tangential injection angle (β) increases, maximum at zero degrees .

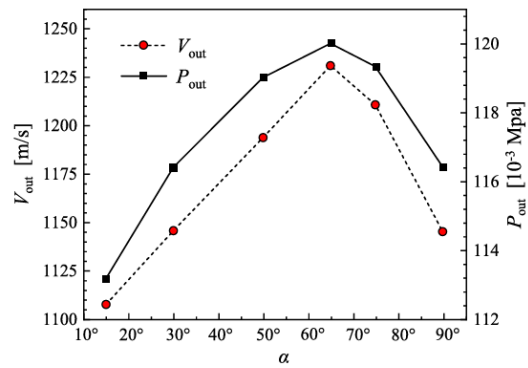


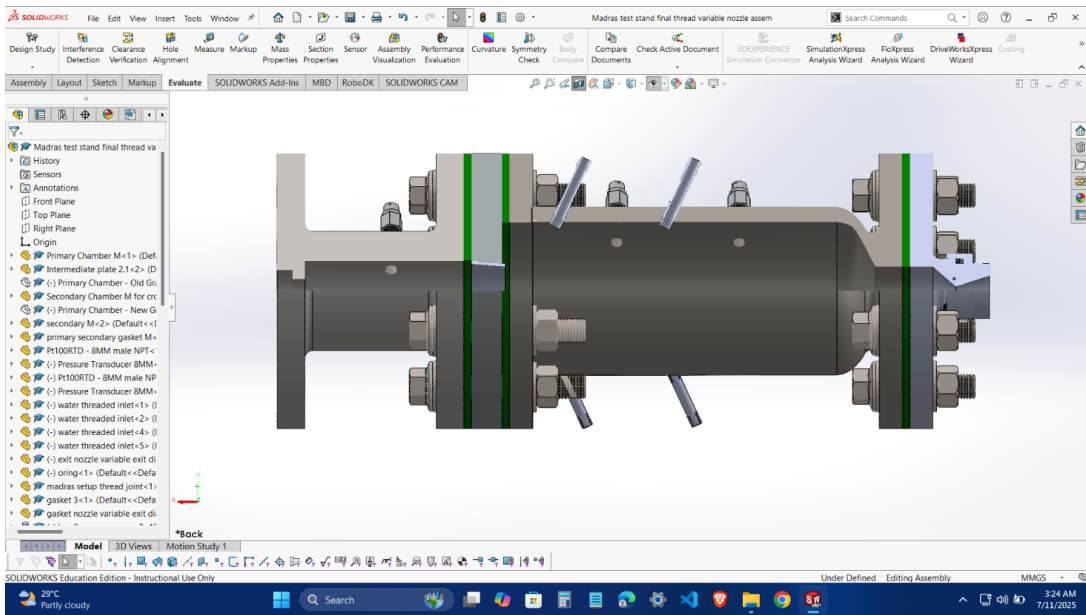
Fig. 13. The variations of outlet velocity V_{out} and outlet pressure P_{out} with axial injection angles α , $R_{w,f1} = 0.4$ and $R_{w,f2} = 1.6$.

(b) Outlet velocity (V_{out}) and pressure (P_{out}) peak at an axial injection angle (α) of around 63 degrees.

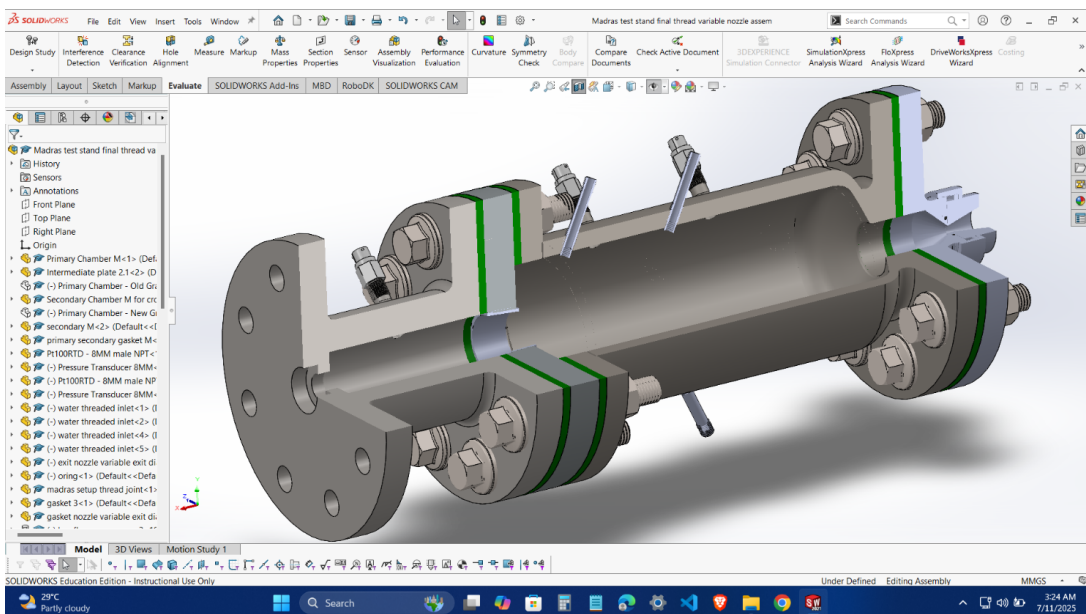
Figure 6.21: Performance graphs from literature illustrating the effect of injection angles.

6.6 Modified Drawings and Features

The initial design drawings were further refined to create a customized horizontal test setup. These modifications introduced several key features, like a simplified intermediate plate, feasible machining of intermediate plate a more practical nozzle insert for the primary chamber, and a precisely controllable variable exit nozzle.



(a) Front view of the modified test bed assembly.



(b) Injection of water at 63 degrees

Figure 6.22: Cross sectional view of modified test bed.

6.6.1 Variable Nozzle Mechanism

A key feature of the modified design is the variable exit nozzle, which allows for different exit diameters and fine-tuning of the exhaust gas flow. This mechanism employs a threaded joint concept, similar to the one initially proposed.

As the external nut is rotated, it pushes the nozzle insert forward, precisely compressing a set of O-rings to create a reliable, leak-proof seal. This design provides a simple yet effective method for adjusting the nozzle's exit diameter during experimental setup.

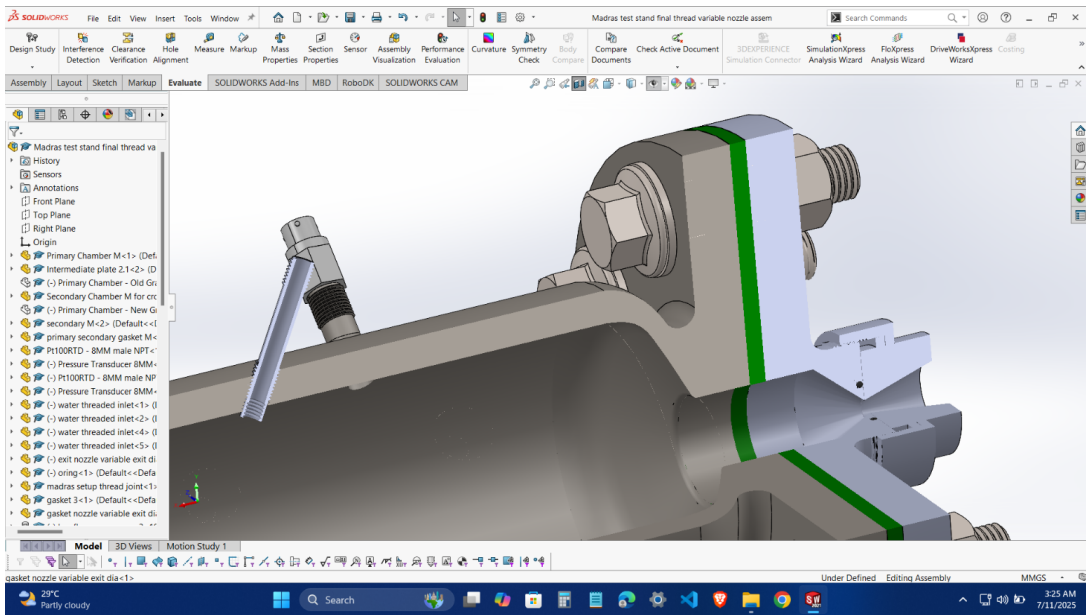


Figure 6.23: A detailed cross-sectional view of the variable nozzle, showing the threaded adjustment mechanism and sealing O-rings.

6.6.2 Modified Primary Chamber Nozzle

To improve manufacturability and allow for easier experimentation, the primary chamber nozzle was redesigned as a simpler, separate insert. This modular approach allows different nozzle geometries to be tested without requiring the fabrication of an entirely new primary chamber.

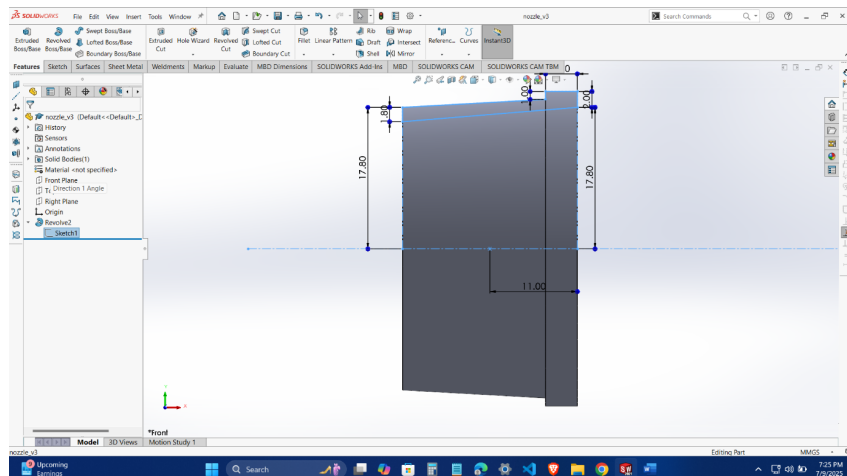


Figure 6.24: Front view dimensions for the modified primary chamber nozzle insert.

Chapter 7

Design Calculations

Calculations were performed for structural integrity (pressure vessel stress), heat transfer (to determine outer wall temperature), and thermal expansion (to ensure proper clearance between the steel chamber and graphite liner). A factor of safety of 4 was used, and the design was validated for the required operational conditions.

Table 7.1: Calculation of Hoop, Radial, and Longitudinal Stresses (σ_y (AISI 1080) = 400MPa)

Primary Chamber									
Ri (m)	Ro (m)	r (m)	Pi (Pa)	Po (Pa)	t (m)	σ_t (MPa)	σ_r (MPa)	σ_l (MPa)	Design Factor
0.030	0.035	0.030	14 184 397.160	101 317.120	0.005	-141.844	919.804	392.799	0.435
0.030	0.045	0.030	14 184 397.160	101 317.120	0.015	-141.844	365.147	113.475	1.095
0.030	0.055	0.030	14 184 397.160	101 317.120	0.025	-141.844	259.110	60.075	1.544
0.030	0.065	0.030	14 184 397.160	101 317.120	0.035	-141.844	216.057	38.394	1.851
0.030	0.075	0.030	14 184 397.160	101 317.120	0.045	-141.844	193.467	27.018	2.068
0.020	0.039	0.020	3 039 513.680	101 317.120	0.019	-30.395	49.337	10.846	8.107
Secondary Chamber									
Ro (m)	Ro (m)	r (m)	Pi (Pa)	Po (Pa)	t (m)	σ_t (MPa)	σ_r (MPa)	σ_l (MPa)	Design Factor
0.045	0.055	0.045	3 039 513.680	101 317.120	0.010	-30.395	147.366	61.550	2.714
0.045	0.060	1.045	3 039 513.680	101 317.120	0.015	36.639	36.888	39.079	10.844
0.045	0.065	2.045	3 039 513.680	101 317.120	0.020	26.004	26.059	27.977	15.350

Identification of Critical Stress Areas

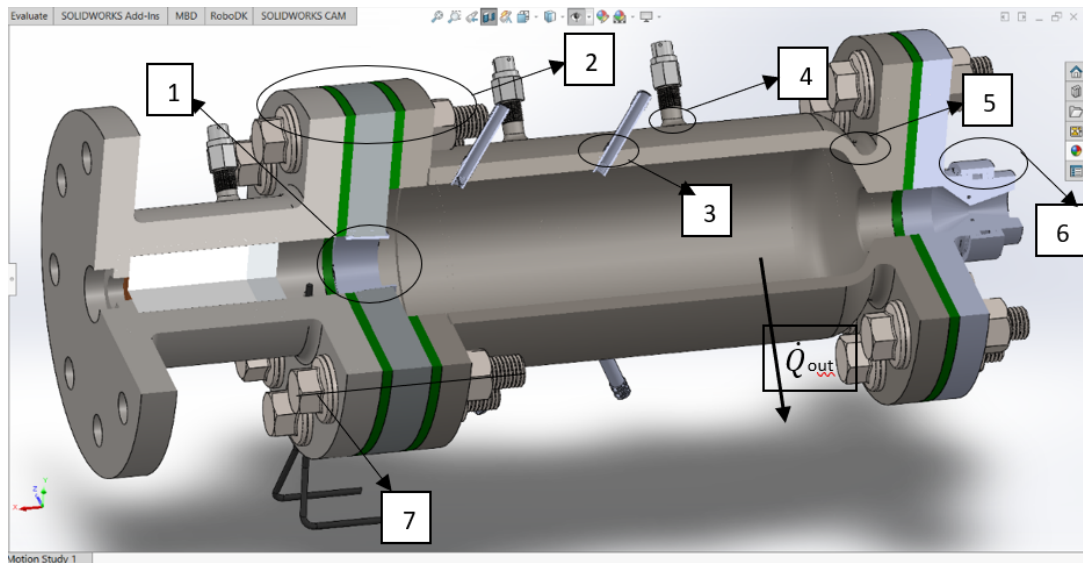


Figure 7.1: Identification of critical stress areas.

Identification of some critical stress areas. The numbered labels in the figure correspond to the following:

- 1 Residual thermal Hoop and Radial Stresses from Interference Fit
- 2 Axial Thermal-Gradient Stress
- 3,4 Axial (Longitudinal) Stress Concentration around Injection Orifices and transducer ports.
- 3,4 Circumferential (Hoop) and Radial Stress Concentrations at Nozzle and transducer Ports
- 5 Stress Concentration at Fillet Radius
- 6 Thermal Stress Concentration at Thread Roots
- 7 Bolt Preload (Tensile) Stress in Fasteners

7.1 Stress Concentration Factor Calculations

To ensure the structural integrity of the design, stress concentration factors (K_t) were calculated for critical geometric features where stress is likely to be amplified. These features include the water injection holes and the fillet at the flange-to-chamber transition.

7.1.1 Stress Concentration near Injection Holes

The injection ports introduce transverse holes in the chamber walls, which act as stress concentrators. The stress concentration factor, K_t , for the hoop stress around these holes was determined using the geometric ratios shown in the table below and referencing the standard chart for a bar in tension with a transverse hole (Figure 7.2).

Table 7.2: Calculation of Stress Concentration Factors at Injection Holes.

Component	w	d	d/w	K_t (hoop)	Description
<i>Primary Chamber</i>					
	0.18526	0.01	0.0539	2.9 (axial)	w is circumference, d is hole depth
		0.12	0.01	0.0833 2.75 (hoop)	w is length of primary chamber
		0.18526	0.019	0.1025 2.7 (radial)	w is circumference, d is hole depth
<i>Secondary Chamber</i>					
	0.3454	0.01	0.0289	3.0 (axial)	w is circumference, d is hole depth
		0.24	0.01	0.0416 2.8 (hoop)	w is length of secondary chamber
		0.3454	0.02	0.0579 2.7 (radial)	w is thickness, d is hole depth

Figure A-15-1

Bar in tension or simple compression with a transverse hole. $\sigma_0 = F/A$, where $A = (w - d)t$ and t is the thickness.

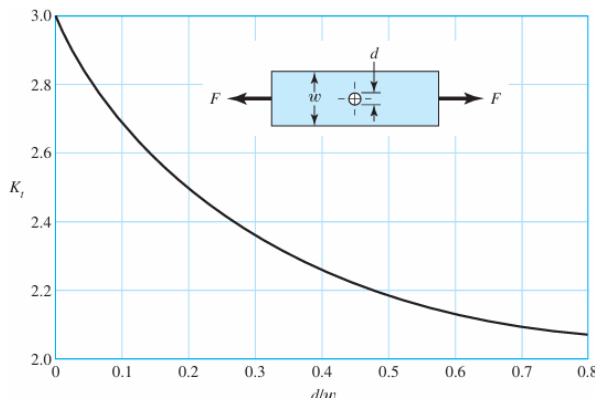


Figure 7.2: Stress-concentration factor (K_t) for a bar in tension with a transverse hole (Figure A-15-1).

7.1.2 Stress Concentration near Fillet to Flange

The transition from the chamber body to the larger diameter of the flange is another critical area. A fillet is used to smooth this transition and reduce the stress concentration. The factor K_t was determined based on the fillet radius (r), the chamber diameter (d), and the flange diameter (D), referencing the standard chart for a shaft with a shoulder fillet (Figure 7.3).

Table 7.3: Calculation of Stress Concentration Factor at the Flange Fillet.

r (mm)	d (mm)	D (mm)	r/d	D/d	K_t
5	32	90	0.156	2.8125	2.2-2.6

Figure A-15-7

Round shaft with shoulder fillet in tension. $\sigma_0 = F/A$, where $A = \pi d^2/4$.

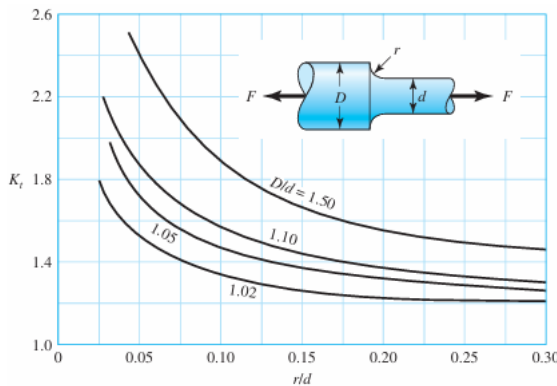


Figure 7.3: Stress-concentration factor (K_t) for a round shaft with a shoulder fillet in tension (Figure A-15-7).

7.2 Failure Theory Analysis

7.2.1 Von Mises Stress Theory

The Von Mises stress theory, also known as the distortion-energy theory, is a widely used criterion for predicting the yielding of ductile materials. It states that yielding begins when the von Mises equivalent stress (σ') is greater than or equal to the material's yield strength (S_y). The von Mises stress is defined as:

$$\sigma' = \left[\frac{(\sigma_1 - \sigma_2)^2 + (\sigma_2 - \sigma_3)^2 + (\sigma_3 - \sigma_1)^2}{2} \right]^{1/2} \geq S_y \quad (7.1)$$

7.2.2 Maximum Shear Stress (MSS) Theory

The Maximum Shear Stress (MSS) theory is a more conservative failure criterion. It predicts that yielding will occur when the maximum shear stress (τ_{max}) in any element is equal to or greater than the maximum shear stress at yielding in a simple tension test ($S_y/2$).

For principal stresses ordered $\sigma_1 \geq \sigma_2 \geq \sigma_3$, the maximum shear stress is:

$$\tau_{max} = \frac{\sigma_1 - \sigma_3}{2} \quad (7.2)$$

Failure is predicted if $\tau_{max} \geq S_y/2$. The factor of safety (n) can be calculated as:

$$n = \frac{S_y/2}{\tau_{max}} \quad (7.3)$$

7.2.3 Failure Analysis Results Table

The following table summarizes the calculated stresses and the resulting design factors for both the primary and secondary chambers based on the Von Mises and MSS criteria.

Table 7.4: Comparison of Design Factors from Von Mises and MSS Theories.

Von Mises Equivalent					
Component	$\sigma_{t,max}$ (MPa)	$\sigma_{r,max}$ (MPa)	$\sigma_{l,max}$ (MPa)	Von Mises Eq. (MPa)	Design Factor
Primary Chamber	83.586	133.210	31.452	88.134	4.538
Secondary Chamber	82.067	397.887	184.650	279.048	1.433
Maximum Shear Stress Criterion (MSS)					
Component	σ_1 (MPa)	σ_2 (MPa)	σ_3 (MPa)		
Primary Chamber	133.210	83.586	31.452		
Secondary Chamber	397.887	184.650	82.067		
Component	$T_{max} = (\sigma_1 - \sigma_3)/2$		$T_{cr} = S_y/2$		Design Factor (MSS)
Primary Chamber	50.879		200		3.931
Secondary Chamber	157.910		200		1.267

* 60 mm outer diameter gives a design factor of 4

7.3 Fatigue Analysis

7.3.1 Theory and Formulas

The fatigue life of a material is often characterized by its endurance limit (S_e) and its S-N curve, which relates stress amplitude to the number of cycles to failure.

Endurance Limit Modifying Factors

The endurance limit (S_e) for a real-world component is obtained by modifying the endurance limit of a pristine test specimen (S'_e) using a set of Marin factors. These factors account for differences in surface condition, size, loading, temperature, and reliability.

$$S_e = k_a k_b k_c k_d k_e S'_e \quad (7.4)$$

where k_a is the surface factor, k_b is the size factor, k_c is the load factor, k_d is the temperature factor, and k_e is the reliability factor.

High-Cycle S-N Line

For high-cycle fatigue (between 10^3 and 10^6 cycles), the relationship between fatigue strength (S_f) and the number of cycles to failure (N) can be modeled by the equation:

$$S_f = aN^b \quad (7.5)$$

The coefficients a and b are determined using the material's ultimate tensile strength (S_{ut}) and the calculated endurance limit (S_e).

7.3.2 Analysis Results

The following table summarizes the calculation of the Marin factors, the endurance limit, and the resulting fatigue life for the primary and secondary chambers made from Steel AISI 1080.

Table 7.5: Fatigue Analysis Calculations and Results.

Marin Factors		
Factor	Value	Notes
k_a	0.7947	$ka=aSut^b$
k_b	1.0000	for axial load
k_c	0.8500	for axial load
k_d	0.5536	for 400C (752F)
k_e	0.8970	for 90% Reliability

Fatigue Life Calculation			
Material	S_{ut} (MPa)	S'_e (MPa)	S_e (MPa)
f	a	b	
Steel AISI 1080	700.0000	350.0000	107.8365
0.8465	3255.9976	-0.2466	

Primary Chamber		
Stress Amplitude (MPa)	No. of Cycles (N)	
2.2799×10^6	(2.27 Million Cycles)	

Secondary Chamber		
Stress Amplitude (MPa)	No. of Cycles (N)	
2.0890×10^4	(20,890 Cycles)	

High-Cycle S-N Line

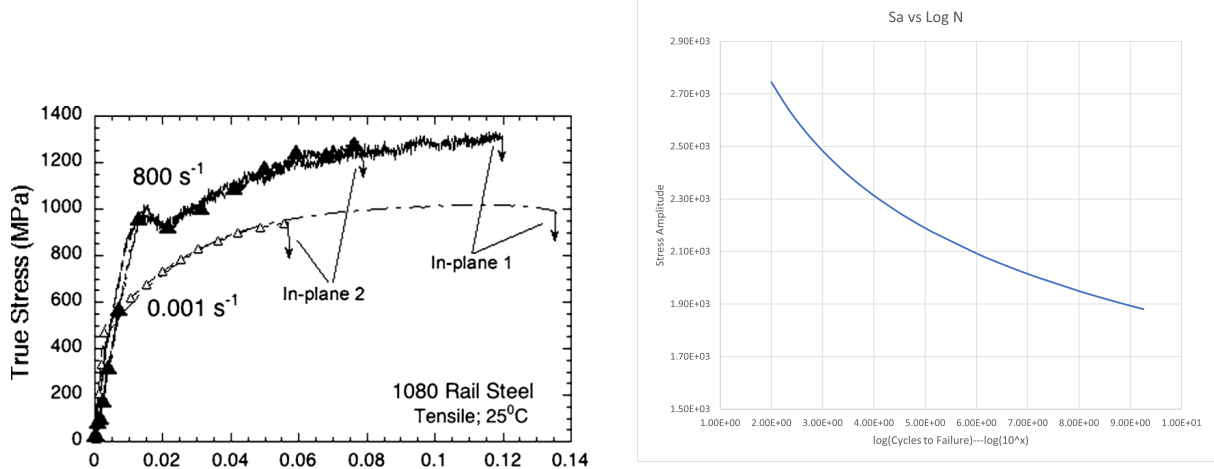
For high-cycle fatigue (between $10^3 < N < 10^6$ cycles), the relationship between fatigue strength (S_f) and the number of cycles to failure (N) can be modeled by the equation:

$$S_f = aN^b \quad (7.6)$$

The coefficients a and b are determined using the material's ultimate tensile strength (S_{ut}), the fatigue strength fraction (f), and the calculated endurance limit (S_e). The formulas are:

$$a = \frac{(fS_{ut})^2}{S_e} \quad (7.7)$$

$$b = -\frac{1}{3} \log \left(\frac{fS_{ut}}{S_e} \right) \quad (7.8)$$



(a) True Stress vs. True Strain curve for 1080 Rail Steel at different strain rates.

(b) The calculated S-N curve (Stress Amplitude vs. log of Cycles to Failure) for the material.

Figure 7.4: Material properties and the resulting S-N fatigue curve.

7.4 Transient Heat Conduction: Lumped Analysis

7.4.1 Theory and Formulas

Lumped analysis is a method used in transient heat conduction that assumes the temperature within a solid body is uniform at any given time. This simplification is valid when the resistance to conduction within the body is much smaller than the resistance to convection at the surface.

The Biot Number

The criterion to apply lumped analysis is determined by the **Biot Number (Bi)**, a dimensionless quantity. Lumped analysis can be applied with good accuracy when the Biot number is less than 0.1.

$$Bi = \frac{hL_c}{k_{solid}} \quad (7.9)$$

where h is the convection heat transfer coefficient, k_{solid} is the thermal conductivity of the solid, and L_c is the characteristic length, defined as the body's volume divided by its surface area ($L_c = V/A_s$).

Temperature Variation with Time

When the lumped analysis condition ($Bi < 0.1$) is met, the temperature T of the body at any time t can be described by the following equation:

$$T(t) = T_\infty + (T_i - T_\infty)e^{-bt} \quad (7.10)$$

Here, T_i is the initial temperature, T_∞ is the ambient fluid temperature, and b is the time constant, given by:

$$b = \frac{hA_s}{\rho c_p V} \quad (7.11)$$

where ρ is density and c_p is specific heat capacity.

7.4.2 Lumped Analysis Calculations

The following table shows the calculation of the Biot number and time constant for the primary and secondary chambers, confirming that lumped analysis is applicable.

Table 7.6: Calculation of Biot Number and Time Constant.

CALCULATION OF BIOT NUMBER							
Component	h (W/m ² K)	k (W/mK)	L_c (m)	Bi	Criterion	Result	
Primary Chamber	10	47.7	0.122	0.02557	< 0.1	Lumped analysis works	
Secondary Chamber	10	47.7	0.240	0.05031	< 0.1	Lumped analysis works	
CALCULATION OF TIME CONSTANT							
Component	h (W/m ² K)	A_s (m ²)	Density	Volume (m ³)	Mass (kg)	c_p (J/kgK)	b (s ⁻¹)
Primary Chamber	10	0.02939	7850	0.000422	3.3158	490	0.000180
Secondary Chamber	10	0.04145	7850	0.000377	2.9579	490	0.000286

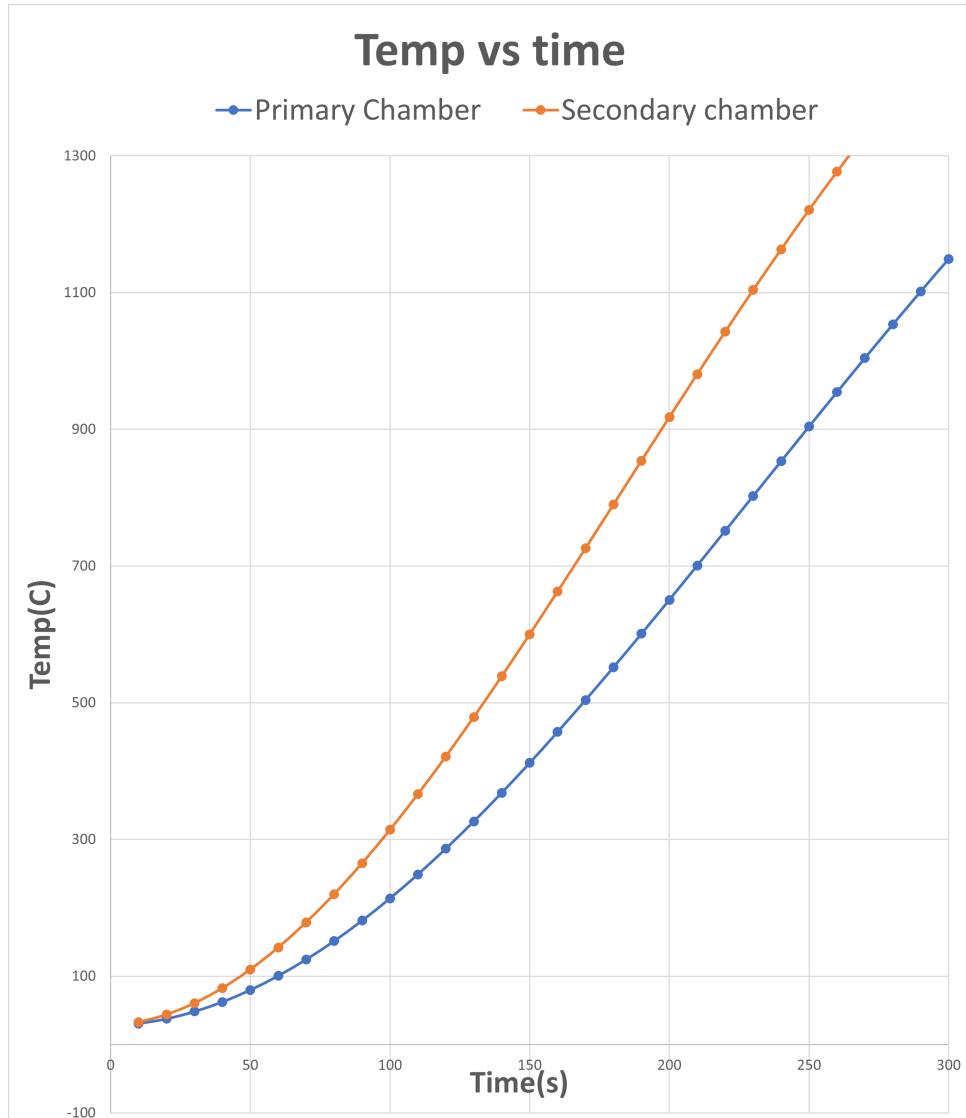


Figure 7.5: Temperature–time response for the primary and secondary chambers, plotted using lumped-analysis. Time constants of $\tau_1 \approx 555$ s (primary) and $\tau_2 \approx 350$ s (secondary).

7.5 Thermal Stress Analysis

7.5.1 Theory and Material Properties

When a material undergoes a temperature change (ΔT), it experiences a thermal strain (ϵ_{th}) defined by its Coefficient of Thermal Expansion (α). If this expansion is constrained, stress develops. The net strain (ϵ_{net}) is the difference between the free thermal strain and any available clearance, and the resulting thermal stress is calculated as $\sigma = E \cdot \epsilon_{net}$, where E is the material's Young's Modulus.

Graphite Properties

- **Compressive Strength:** The room-temperature compressive strength of NBG-18 graphite was reported as 80 MPa by Béghin et al. Carroll et al., using ASTM C695-91 test standards, determined a mean compressive strength of 81.28 ± 4.34 MPa from 260 test specimens.
- **Coefficient of Thermal Expansion (CTE):** The CTE of polycrystalline graphite is not linear with temperature. The average CTE measured over 20–100 °C can be extrapolated to higher temperatures by applying a temperature-dependent correction term. For the graphite used in this analysis, a value of $14 \mu\text{m m}^{-1} \text{ }^\circ\text{C}^{-1}$ is adopted.

7.5.2 Thermal Stress Calculation Results

The following table details the thermal stress calculations for the primary nozzle, intermediate plate, and secondary nozzle under various operating conditions.

Table 7.7: Thermal Stress Analysis Results for Key Components.

Component	C _{TE} (μm/m-°C)	ΔT (K)	Clearance (mm)	Free Strain (ε _{th})	c Strain (ε _c)	Net Strain (ε _{net})	Young's Modulus (Gpa)	Thermal Stress (Gpa)	Yield Strength (Gpa)	Design Factor
PRIMARY NOZZLE (Graphite Data)										
14	1000	0.30	0.008427	0.0140	-0.005573	16	0.089169	0.08	0.8972	
14	1000	0.35	0.008887	0.0140	-0.005113	16	0.081798	0.08	0.9780	
14	1000	0.40	0.009831	0.0140	-0.004169	16	0.066697	0.08	1.1995	
14	1000	0.45	0.011260	0.0140	-0.002740	16	0.044247	0.08	1.8080	
14	1000	0.48	0.012576	0.0140	-0.001424	16	0.023160	0.08	2.7741	
14	2000	0.80	0.022472	0.0280	-0.005529	16	0.088449	0.08	0.9045	
14	2000	0.90	0.025809	0.0280	-0.002191	16	0.043506	0.08	1.8388	
14	2000	0.95	0.026636	0.0280	-0.001364	16	0.021834	0.08	3.8034	
INTERMEDIATE PLATE (AISI 1080 Data)										
13.7	800	0.20	0.005480	0.1036	-0.005342	205	1.111421	0.4	0.3600	
13.7	800	0.30	0.008207	0.1036	-0.002532	205	0.529400	0.4	0.7556	
13.7	800	0.35	0.009314	0.1036	-0.001164	205	0.236933	0.4	1.6670	
13.7	800	0.38	0.104742	0.1036	0.000086	211	0.006810	0.4	6.6211	
SECONDARY NOZZLE										
14	2000	0.80	0.022472	0.0280	-0.005529	16	0.088449	0.08	0.9045	
14	2000	0.90	0.025281	0.0280	-0.002719	16	0.043506	0.08	1.8388	
14	2000	0.95	0.026636	0.0280	-0.001365	16	0.021834	0.08	3.8034	

Chapter 8

Simulation

8.1 Simulation

To verify the analytical calculations and gain a deeper understanding of the component's behavior under operational loads, a preliminary Finite Element Analysis (FEA) was conducted using Ansys.

8.1.1 Analysis simulation Procedure

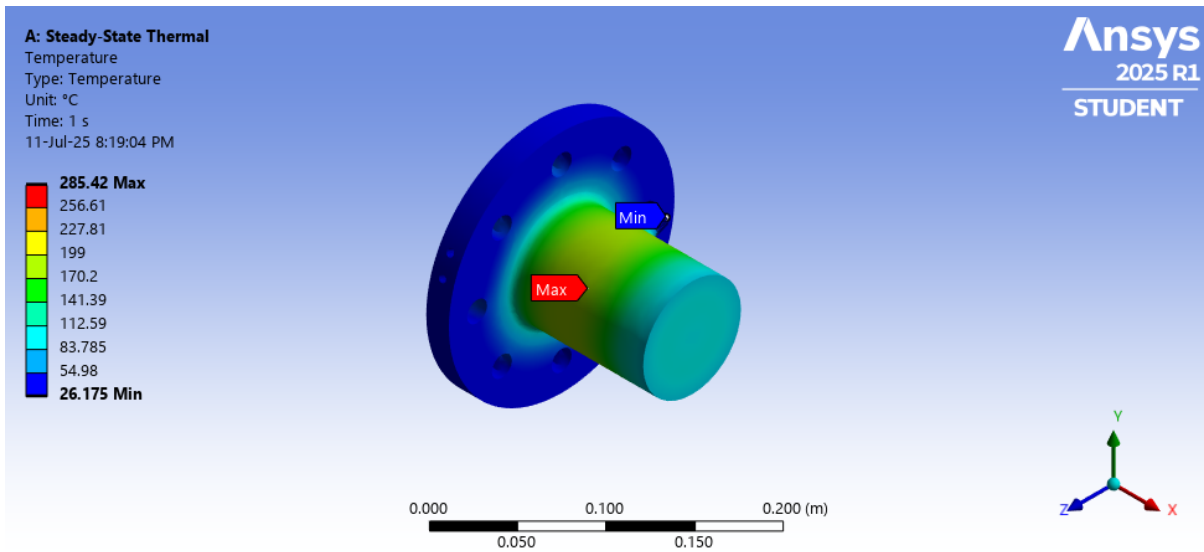
The simulation consisted of two main steps:

1. A **Steady-State Thermal Analysis** was performed to determine the temperature distribution throughout the component under constant thermal loads.
2. The resulting temperature field was then imported as a load into a **Static Structural Analysis** to calculate the equivalent (von-Mises) stress caused by thermal expansion.

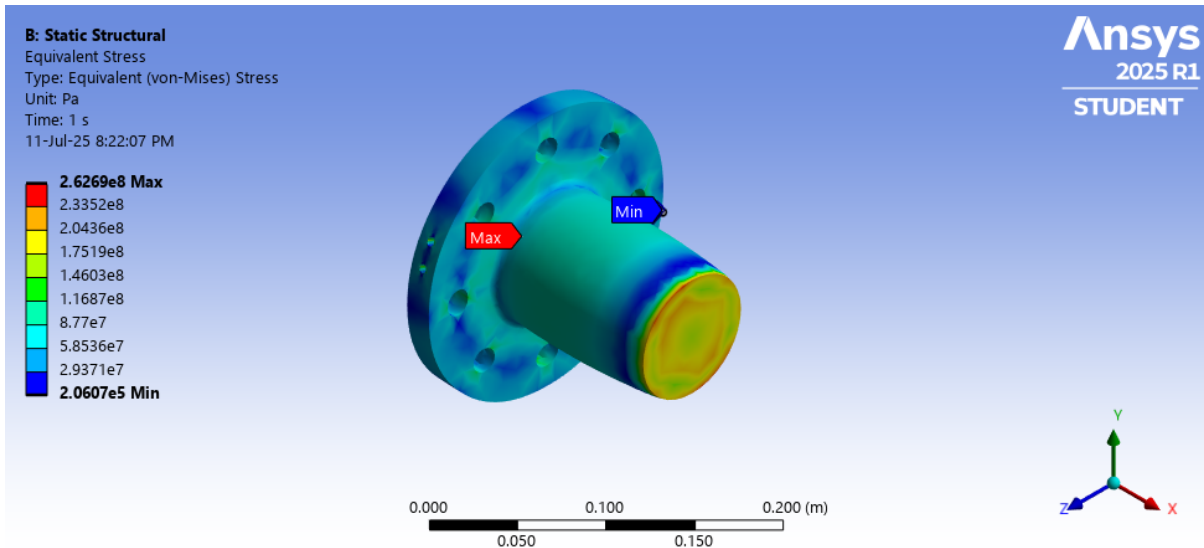
It is important to note that these simulations were performed using a relatively **coarse mesh**. While this approach is useful for identifying general trends and potential high-stress regions, the results are not highly accurate. For precise, quantitative results, a more detailed analysis with a finer, more refined mesh would be required.

8.1.2 Simulation Results

The results from the thermal and structural analyses are presented below.



(a) Steady-State Thermal Analysis, showing a temperature distribution from 26.175°C to a maximum of 285.42°C at the inner fillet.



(b) Static Structural Analysis, showing the resulting Equivalent (von-Mises) Stress. The maximum stress of 262.7 MPa occurs at the inner fillet.

Figure 8.1: Preliminary FEA results for the primary chamber flange, showing temperature and stress distributions.

Chapter 9

Views of the Test Bed

This section presents various orthographic and isometric views of the test bed assembly to understand its construction.

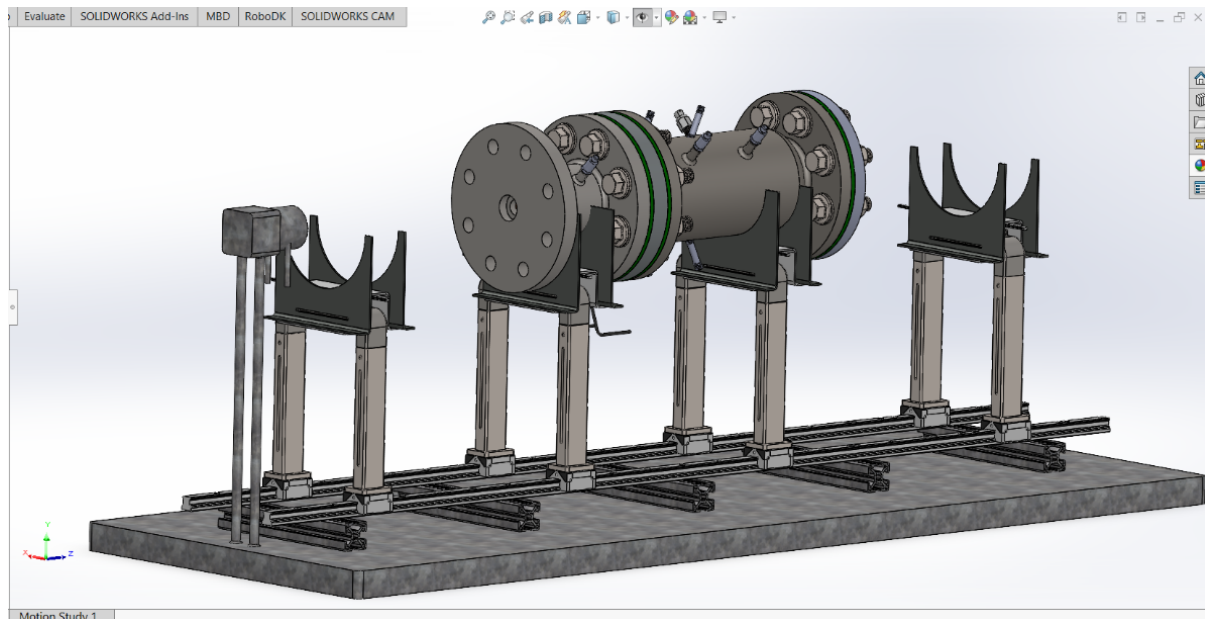


Figure 9.1: Isometric view of the full test bed assembly, the pressure chamber mounted on the adjustable supports and linear guide rail.

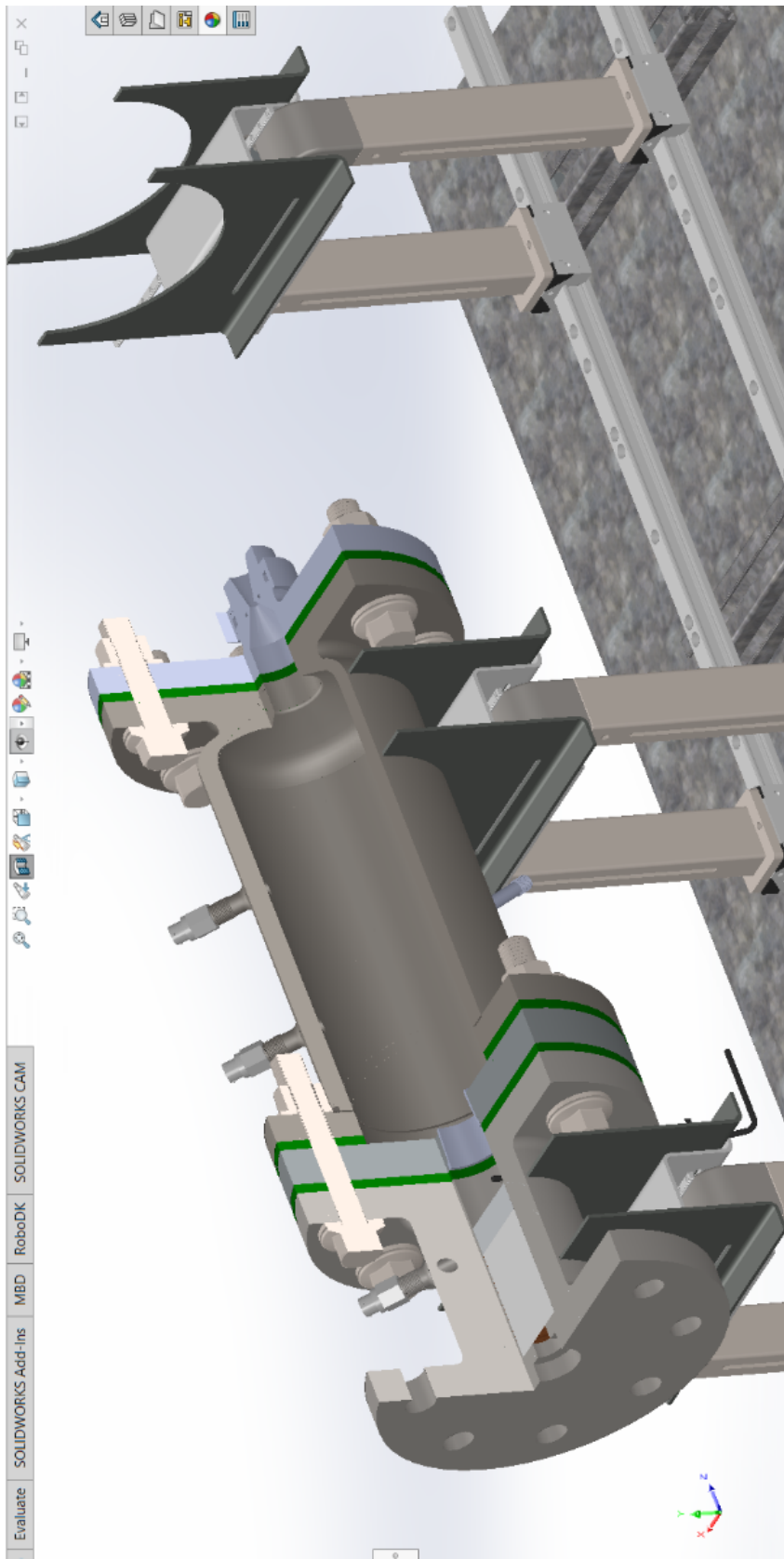
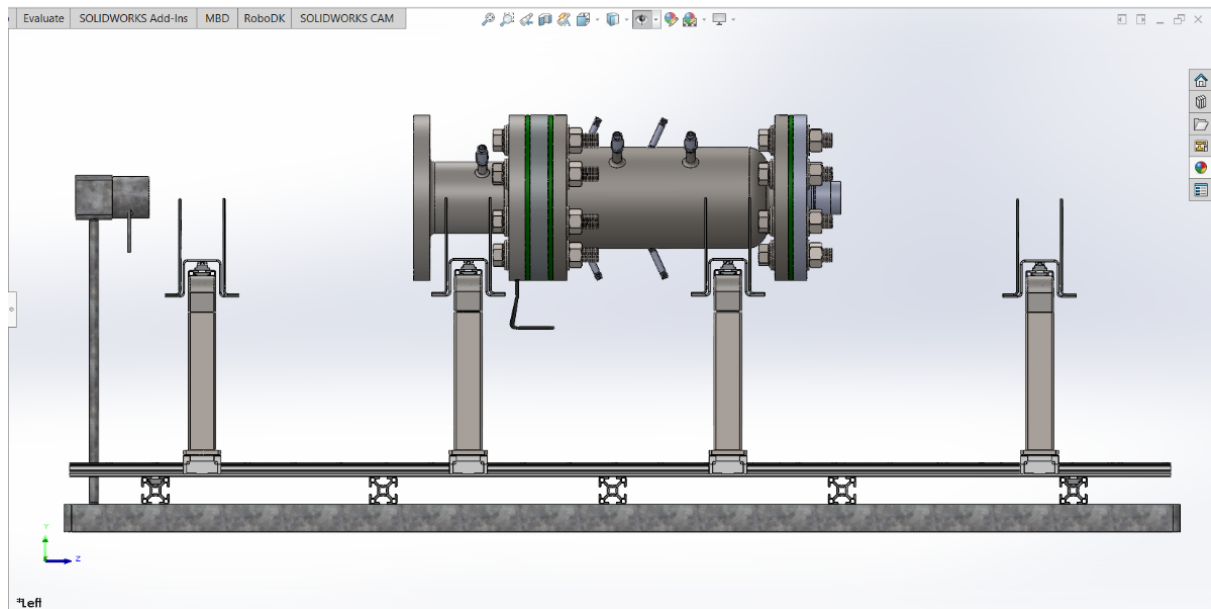
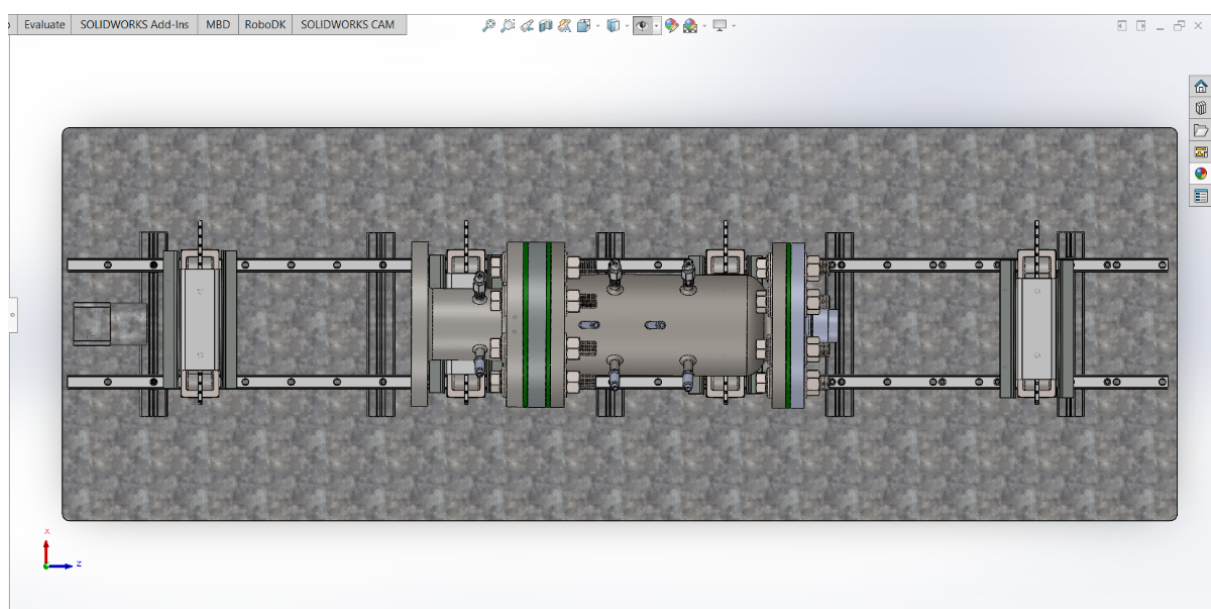


Figure 9.2: A partially sectioned isometric view, highlighting the pressure chamber, intermediate plate and nozzle assembly

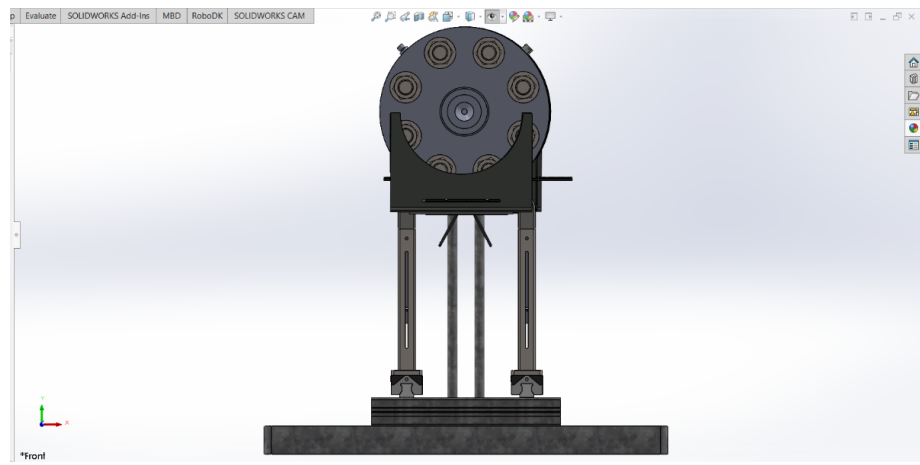


(a) Side elevation view of the test bed.

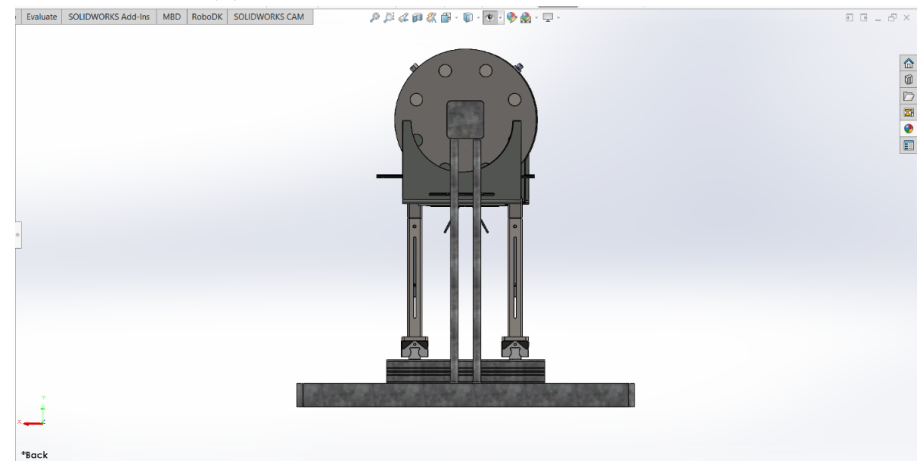


(b) Top plan view of the assembly.

Figure 9.3: Orthographic side and top views of the test bed assembly.



(a) Front view, showing the main flange.



(b) Rear view of the test bed assembly.

Figure 9.4: Orthographic front and rear views of the assembly.

Conclusions

In the first part of my work, I learned the basics of making solid rocket fuel by mixing binders, oxidizers, and metal powders. I saw how changing particle sizes or the order of mixing could make the fuel stronger or burn more evenly. I tackled issues like uneven mixing by testing small batches and adjusting my methods. I have understood some fundamental concepts of solid rocket propulsion, how this exothermic chaos is carefully controlled and engineered to serve as a reliable propulsive device, and I have really felt the extreme importance of precision in engineering to keep this delicate dance of chaos in control. How minor inconsistency in composition can have completely different outcomes.

I learned basic principles of calorific value measurement and measured how much energy the fuel released using a bomb calorimeter, and tracked how fast it burned in a strand-burner and studied the equations governing it. When the data didn't match my expectations, I learnt to break the problem into fundamentals and find the point responsible for error.

I have explored new ways of working hydrogen, and stormed on intricacies posed by it, and worked on several complex injections but conclude simple is always better. I faced seal failures and clogging problems, but by trying new materials and adjusting flow rates, I addressed them.

Harnessing additional energy from the oxidizer from the surrounding medium will improve specific impulse. I have learnt several concepts like relating composition and burn rates to chamber pressure to motor and some insights into nozzle, and how different grain geometries affect the overall thrust profile. I have honed my CAD and design skills while designing the hydro reactive test bed, I have explored several configurations and designs to achieve the desired functionality (gaskets, threaded joints), and aimed for best feasible design to manufacture. I have also prepared the bill of materials simultaneously to bring the setup from CAD to real world in lab. Manufacturability was my main focus at every step of design.

Finally, using the Open Motor simulation tool helped me connect theory with practice. By entering grain shapes, burn-rate data, and nozzle sizes, I could predict thrust and pressure before any test. When the simulated results didn't match the experiments, I was driven to refine my models and understand the discrepancies.

This blend of hands-on work on fabricating real projects and computer modeling has strengthened my engineering skills; it has shown how vast the knowledge base is to be required to design such setups which fueled my passion to learn and explore more and gain knowledge in various software, courses and new subjects, some hard problems had taught so much resilience and prepared me to tackle future challenges with confidence. I am grateful for the opportunity to learn with exceptional people.

Thank you, sir.

References

- [1] Sutton, G. P., & Biblarz, O. (2016). *Rocket Propulsion Elements* (9th ed.). Wiley.
- [2] Mishra, D. P. (n.d.). *Fundamentals of Rocket Propulsion*.
- [3] Murugesan, R. (2023). *Investigation on hydro-reactive fuel powered water-breathing jet propulsion for high-speed underwater vehicles* (Doctoral thesis, Department of Aerospace Engineering, Indian Institute of Technology Madras).
- [4] Yavora, Y., Goroshin, S., Bergthorson, J. M., Frost, D. L., Stowe, R., & Ringuette, S. (2021). Enhanced hydrogen generation from aluminum–water reactions. *International Journal of Hydrogen Energy*.
- [5] Mutlu, R. N., Kandasamy, J., Kiyamaz, T. B., Gülcü, D., Böncü, E., Eroglu, E., & Gökalp, İ. (2020). Optimization of aluminum hydrolysis reactions and reactor design for continuous hydrogen production using aluminum wire feeding. *TÜBİTAK MAM Clean Energy Technologies Reports*.
- [6] MatWeb. (n.d.). *Zirconium alloy C 103, sheet and plate* [Data sheet]. Retrieved July 18, 2025, from <https://www.matweb.com/search/datasheet.aspx?matguid=37ca3458dfbe482fbe1efdf59d52e424&ckck=1>
- [7] Nakka Rocketry. (n.d.). *Thermochemical properties of hybrid propellants*. Retrieved July 18, 2025, from https://www.nakka-rocketry.net/th_imp.html
- [8] Huang, L., Xia, Z., Hu, J., & Zhu, Q. (2011). Performance study of a water ramjet engine. *Journal of Propulsion Science and Technology*, 30(2), 123–130.
- [9] Hashish, A. E. A. (2018). *Design of solid motor for predefined performance criteria* (Master's thesis, Military Technical College, Cairo).
- [10] Nakka, R. A. (1984). *Design of a hybrid rocket motor for predefined performance criteria* (Bachelor's thesis, University of Manitoba).
- [11] Reilley, A. (n.d.). *OpenMotor* [Software]. GitHub. Retrieved July 18, 2025, from <https://github.com/reilleya/openMotor>
- [12] Google Slides. (n.d.). *OpenMotor burn rate editor overview* [Presentation]. Retrieved July 18, 2025, from https://docs.google.com/presentation/d/172XP59fQkP5xur5ILQIjTvHPt_BzAXesqwsQp6cBUM/edit
- [13] Mahajan, D. K. (n.d.). *Machine Design (ME304)* [Course materials]. Department of Mechanical Engineering, Indian Institute of Technology Ropar.